Optimizing Printing Fidelity of the Single-Nozzle Based Multimaterial Direct Ink Writing for 3D Food Printing

By Zhennan Tian

Supervisors **Prof. Haonan Li**

Dr. Chung Ket Thein

Dr. Kean How Cheah

A master thesis submitted for the degree of Master of Mechanical Engineering of Nottingham University

Department of Mechanical, Materials, and Manufacturing Engineering

May 2024

(This page is left blank)

Abstract

Direct Ink Writing (DIW) is an extrusion-based layer-by-layer printing technique that involves pressure-driven deposition of a viscoelastic ink through a fine nozzle, which is widely recognized as the most effective technique in 3D Food Printing (3DFP) research. This thesis explores the optimization of printing fidelity in pneumatic-driven single-nozzle based multimaterial DIW for 3D food printing applications. Specifically, this study addresses critical challenges inherent to single-nozzle configurations, i.e., the problem of residual material in the shared channel which adversely affects printing fidelity. We introduce an innovative path planning algorithm designed to mitigate these challenges by implementing an advanced distance compensation strategy and in-process printhead motion adjustments, thereby stabilizing the extrusion process during material switching.

The results demonstrate an improvement in printing fidelity. The optimization of advanced distance compensation reduced the offset at switching points to a precision of ±0.5 mm, and the optimization of printhead movements decreased unstable extrusion behaviors, specifically bulging and necking, by 27±5% and 19±3%, respectively.

This research paves the way for more sophisticated applications of DIW in food science, potentially transforming food design and manufacturing processes by improving the fidelity and efficiency of multimaterial printing.

Acknowledgement

I would like to express my sincere gratitude to Prof. Haonan Li. His meticulous guidance has been instrumental in completing this research work for my master's thesis. Throughout my pursuit of the master's degree, I have deeply appreciated Prof. Li's keen academic insight, rigorous scholarly approach, relentless spirit of progress, and his caring and approachable demeanor. His ability to pinpoint research issues and provide rational advice during our discussions on the project's progress has been invaluable. He has led by example, encouraging, educating, and guiding me, not only imparting knowledge but also setting a shining example for my own learning. Prof. Li's support in terms of experimental funding and academic paper writing has made me feel incredibly fortunate and grateful. Completing this master's thesis under the care and guidance of my mentor has been of utmost significance to me.

I am also deeply thankful to Dr. Yinfeng He from the China Beacons Institute at the University of Nottingham Ningbo China. Dr. He has not only imparted a wealth of knowledge in 3D printing technologies but has also meticulously guided my academic writing and research methodologies. His dedication to excellence and his patient instruction have significantly shaped my professional and personal growth. His insights and encouragement were crucial in navigating the challenges of my research. I sincerely thank Dr. He for his unwavering support and invaluable contributions to my academic development.

Finally, I am deeply grateful to my family members for their support and understanding. I will dedicate my entire life to repay their kindness.

Originality Statement

I hereby declare that all the other efforts in this academic dissertation are taken by myself under the guidance of my supervisors. To the best of my knowledge, the work presented in this dissertation is original and does not contain any research achievements published or written by others.

田振楠

2024.5.28

Author signature & Date

Publications

Paper accepted

Tian, Z., Zhong, Q., Zhang, H., Yin, T., Zhao, J., Liu, G., Zhao, Y., **Li, H.**, & **He, Y.** (2024). Optimising printing fidelity of the single-nozzle based multimaterial direct ink writing for 3D food printin. *Virtual and Physical Prototyping*, *19*(1), Article e2352075. Advance online publication.

https://doi.org/10.1080/17452759.2024.2352075

Patents accepted

Gongyu Liu, **Zhennan Tian**, Tianze Yin, Jinxi Zhao, Haonan Li. A printing control method and system for multimaterial single-nozzle based printer. CN117207531A 2023.12.12

Haonan Li, Zhongjie Deng, **Zhennan Tian**, Yinfeng He, Jinxi Zhao, Tianze Yin, Gongyu Liu. A multimaterial single-nozzle based 3D printer. CN202322471589.0 2024.04.26

Yongjie Zhao, Kexing Huang, **Zhennan Tian**, Kunyang Li, Qinfeng Li. A pneumatic driven extrusion multimaterial suspension 3D printer. CN220661543U 2024.03.26

List of Figures

Figure 2-4 DIW applications. a-i) Schematic illustration of direct-write assembly of interdigitated micro-battery architecture. (ii) Schematic of the tactile sensor consisting of a base layer, top and bottom electrodes, an isolating layer, a sensor layer, and a supporting layer. (iii) Photograph of silver interconnects on a 4-by-4 LED chip array. (iv) Photograph of a printed antenna. b-i) 90°/0° Flower morphologies generated by biomimetic 4D printing. (ii) Comparison between printed hemitoroidal shell structures at room and 200 °C temperature. c-i) Photograph of the coaxial printhead connected to the core, interface, and shell ink reservoirs. (ii) Schematic of the progressive alignment of high aspect ratio fillers within the nozzle and triangular honeycomb structures composed of SiC-filled epoxy. d) Chocolate with plant sterol powder and different infill patterns; cookie dough (with xanthan gum) before and after baking; vitamin-D enriched orange concentrate with wheat starch and k-carrageenan; printed lemon juice gel in ring shape; meat. e-i) A doll face is scanned and coated with a 4.5 wt% Flink solutio. (ii) Schematic of cardiac and muscle structure, and images of aligned microfibers in a polycaprolactone mesh and cellular alignment in a cultured environment. (iii) Images of 3D-printed microvascular networks showing the intricate network channels and their fluorescent imaging.

Figure 2-5 Coaxial nozzle extrusion. A) The surimi-based imitation crab meat; B) artificial meat; C) customized food produced by nanoemulsion; D) snacks rich in microalgae.

Figure 2-6 A) Cookie with and embedded extruded C shaped and double-nozzle printed celery turkey cube structure; B) Liquid chocolate-based ingredients; C) Milk and chocolate and other ingredients; D) Mashed potatoes/strawberry juice gel; E) 3D printed composite multi-layer meat; F) RCJ-V-PS and lemon juice gel; G) Mashed potatoes/purple sweet potato puree; H) lotus root powder gel; I) Purple potato puree/oleogel; J) Mooncakes with filling; K) Qingtuan.

Contents

Chapter 1 Introduction

1.1 Background

3D food printing (3DFP) has attracted considerable interest for its ability to create customized foods with appealing geometries, enhanced sustainability, as well as functional foods designed for specific dietary need, that were previously difficult or impossible to achieve with traditional food processing techniques.

This technology is particularly attractive for its potential to control the spatial distribution of ingredients like salt and sugar, supporting reduced intake of these substances without compromising taste. This innovations in 3DFP could assist in managing health conditions such as diabetes and cardiovascular diseases by facilitating controlled diets.

Direct Ink Writing (DIW), an extrusion-based method, is widely recognized as the most effective technique in 3DFP research. It handles a wide range of materials, including protein-rich hydrogels and complex carbohydrates, essential for versatile food printing. DIW also enables the precise creation of complex food structures, thanks to its robust extrusion capabilities. These strengths make DIW particularly suitable for 3DFP, where detailed geometrical designs and customized nutritional content are key requirements.

Traditional DIW is limited to extruding only one material with each printhead, which requires multiple printheads for multi-material printing. This is inefficient due to high material switching times caused by the printheads switching between different materials at each layer. However, existing multimaterial 3DFP methods often use multiple nozzles, which hampers the promotion of multimaterial 3DFP in real life due to the inefficient switching (Figure 1-1c), increased equipment costs and the need for precise calibration. These problems lead to low efficiency in multimaterial 3DFP, high equipment and maintenance costs, which hamper the widespread of practical applications.

To address these challenges, a multimaterial DIW system for 3DFP (Figure 1-1a) would be to enable the continuous extrusion of multiple materials, adjusting compositions on-the-fly to create intricate, voxelated structures (Figure 1-1b). This capability would not only match the precision of inkjet printing but also surpass its material limitations, leveraging DIW's broader material compatibility. Hardin *et al.* [1] and Skylar-Scott *et al.* [2] originally proposed a printhead design that incorporates multiple input channels and one shared nozzle, facilitated by a microfluidic chip-like printhead, which significantly improves the printing speed of complex multimaterial structures. It allows for in-process material switching through a shared nozzle, effectively reducing switching times and simplifying machine operation. This can improve the efficiency of multimaterial 3DFP and reduce equipment costs, effectively promoting the practical application.

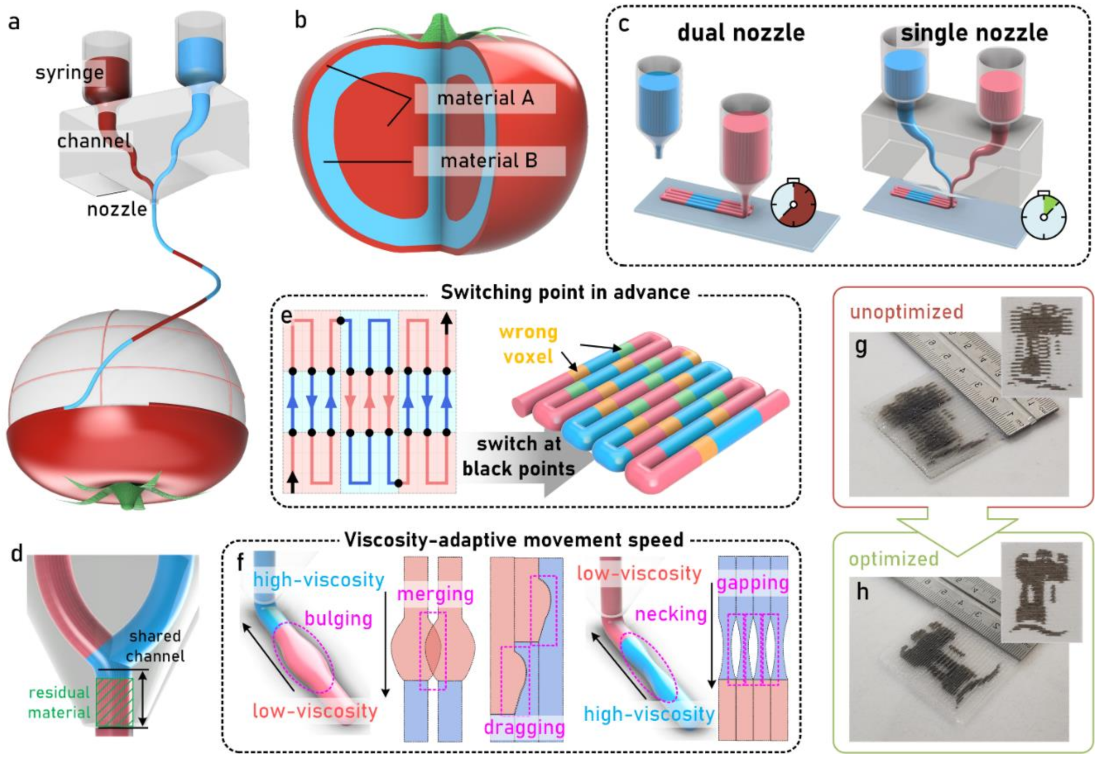

Figure 1-1 a) *Schematic of single-nozzle based MM-DIW printhead design for food 3D printing;* ***b)*** *exemplar of using MM-DIW to fabricate food with customized ingredient designs;* ***c)*** *Comparison of printing efficiency between dual-nozzle and* *single-nozzle based MM-DIW process;* ***d)*** *The shared channel and residual material at the switching point in single nozzle based MM-DIW;* ***e)*** *Schematic of unoptimized path and the corresponding printed chessboard;* ***f)*** *Schematic of defects caused when switching between materials of different viscosity;* ***g)*** *Printed logo pattern with unoptimized path;* ***h)*** *Printed pattern with optimized path.*

Due to the viscosity of the materials used in the 3DFP are always large, pneumatic-driven DIW is preferred and this method is more economical and easier to promote. However, pneumatic-driven method can only set a few fixed air pressure to control pressure on or off, and cannot directly and accurately control the extrusion flow rate. Therefore, this single-nozzle based method still has challenge:

(a) when different materials pass through the shared channel (Figure 1-1d), residual material from previous extrusions can cause delays and inaccuracy in the deposition of the next material (Figure 1-1e).

(b) Materials with differing rheological properties require distinct extrusion pressures and printhead movement speeds, leading to complications at material switching points (Figure 1-1f).

Lee *et al.* [3] presented these challenges in their recent manuscript, which can seriously disturb the printing fidelity, resulting in disagreements between the final printed product and its intended design, and the printed part failure such as pattern discrepancy or ingredients cross-contamination.

1.2 Objectives and Thesis Structure

This thesis aims to apply single-nozzle based multimaterial DIW to 3DFP and improve the accuracy (Figure 1-1g & h) and reliability to make it more suitable for 3DFP process. To overcome the previously mentioned challenges that lead to insufficient performance, this thesis investigates the underlying defects and introduces a path planning algorithm to mitigate these errors. The approach includes (a) the implementation of calculated advance distance at material switching points to offset extrusion delays, and (b) the adjustment of printhead movement speed to align with real-time flow rates, thereby addressing flow instability when switching materials. Recognizing the absence of existing slicing strategies that incorporate the above two optimizations, we propose an integrated slicing algorithm that encompasses both solutions. This enables accurate distribution of ingredients and enhances the stability and success rate of printing, which is crucial for 3DFP where there is often a large difference in material viscosity. It is also important for the practical application of multimaterial 3DFP.

The outline of each chapter (Figure 1-2) is as follows:

Chapter 2: Literature Review introduces a detailed review on (i) multimaterial direct ink writing (DIW) including multiple-nozzle sequential method and single-nozzle continuous method, and (ii) 3D food printing (3DFP) via DIW.

Chapter 3: Methodology introduces the general research methodology from the aspects of (i) mechatronics design of a single-nozzle based multimaterial DIW system for 3DFP, (ii) materials preparation for evaluations and food printing experiments, (iii) a novel slicing algorithm for single-nozzle based multimaterial DIW, and (iv) optimization models which address the issues of low accuracy in the printing process.

Chapter 4: Result & Discussion introduces (i) evaluation of the optimization model's performance, (ii) the printing results of the common scenes, and (iii) the printing results of the food products.

Chapter 5: Conclusions summarize the research outcomes and present future works for this thesis.

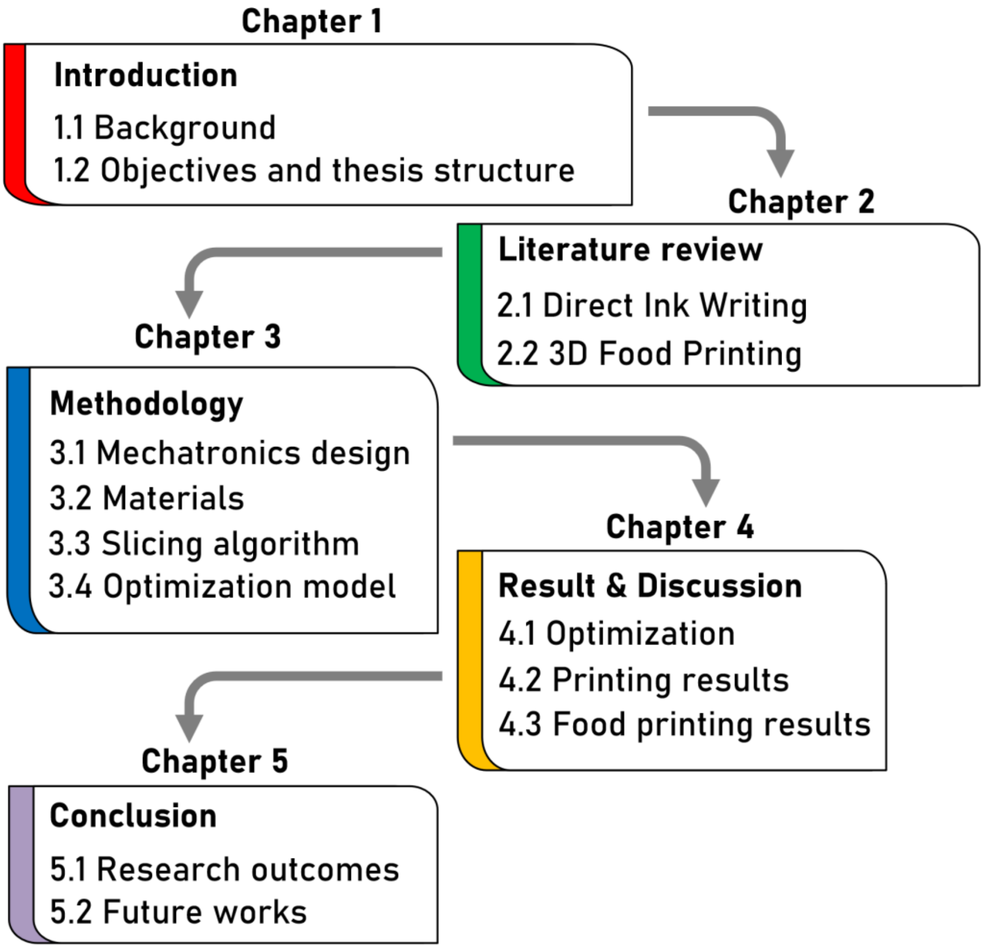

Figure 1-2 *Thesis structure.*

Chapter 2 Literature Review

2.1 Additive Manufacturing

Additive manufacturing (AM), commonly known as 3D printing, involves creating three-dimensional objects by adding material layer by layer, allowing for complex designs not possible with traditional manufacturing. Originating in the 1980s, this technology enables high customization and is used in diverse industries such as aerospace, automotive, healthcare, and fashion. AM techniques are classified according to ISO ASTM 52900:2015 [4] into seven primary categories:

Vat Photopolymerization: Uses a light source to cure liquid resin in a vat layer by layer.

Powder Bed Fusion: Involves either a laser or electron beam to melt and fuse material powder together.

Binder Jetting: Uses a liquid binding agent to join powder materials.

Sheet Lamination: Layers of material are bonded to form an object.

Material Jetting: Drops of photopolymer are jetted and cured by light.

Directed Energy Deposition: Focuses thermal energy to fuse materials as they are being deposited.

Material Extrusion: Material is selectively dispensed through a nozzle or orifice.

Direct Ink Writing (DIW) belongs to material extrusion, extruding a viscous ink through a nozzle, layer by layer, to build 3D structures.

2.2 Direct Ink Writing

Direct Ink Writing (DIW) is an extrusion-based layer-by-layer printing technique that involves pressure-driven deposition of a viscoelastic ink through a fine nozzle. The process involves three main steps: 1) Creating 3D models with Computer-Aided Design (CAD) software, 2) Generating nozzle movement paths via slicing software, and 3) Depositing the ink [5]. This technique allows customization of inks to achieve high precision in printing 3D structures on meso- and microscales. Critical factors like nozzle size and printing speed affect resolution and accuracy, with resolutions ranging from 100–1200 µm in the x–y plane and 100–400 µm in the z-direction; the minimum feature size is about 500 µm [6]. Smaller nozzles enhance resolution but require higher extrusion pressures and longer build time due to potential clogging risks. Conversely, slower speeds improve shape fidelity but increase printing duration. DIW's key feature is its ability to extrude inks at room temperature, relying on the ink’s rheological properties rather than temperature. Optimizing ink rheology is vital and involves adjustments like chemical modifications and adding rheological modifiers and fillers [7, 8]. During printing, the ink filament stretches and bends slightly, which can be managed by adjusting the extrusion rate to printing speed ratio (printhead movement ≈ 5–50 mm s^{-1}). Solidification of the ink occurs through natural settling or external means such as solvent evaporation, gelation, or photocuring [5]. DIW offers minimal post-processing and reduced material waste, enhancing both the sustainability and economy of the manufacturing process.

2.2.1 Principles of direct ink writing

DIW employs various extrusion methods to dispense materials effectively, tailored by the physical properties of the ink. These methods can be categorized into pneumatic-driven, piston-driven, and screw-driven extrusion systems, each suitable for different types of materials and applications.

Pneumatic-driven Extrusion: In the pneumatic-driven extrusion system, compressed air is used to dispense the ink (Figure 2-1a). The system typically consists of a syringe filled with the ink material, which is connected to an air pump through an adapter and tubing. This method is particularly effective for materials that can maintain their form after extrusion, such as certain gels. To ensure a clean and consistent extrusion, it is essential to manage the air pressure precisely and to use filters to prevent contamination.

Piston-driven Extrusion: The piston-driven system offers a robust solution for extruding materials with higher viscosities, such as thick pastes or polymers. This system operates through a motor-driven piston that moves within a cylinder to push the material through a nozzle (Figure 2-1b). The controlled movement of the piston allows for precise dispensing of the material, making it suitable for creating detailed and structured outputs.

Screw-driven Extrusion: Similar to the piston-driven method but designed for even greater control and pressure, the screw-driven system uses a screw mechanism connected to a motor to extrude the material (Figure 2-1c). This method is advantageous for very viscous materials and offers enhanced volumetric control. However, the mechanical nature of the screw can potentially affect the integrity of sensitive materials, thus requiring careful design and operation to minimize any damaging effects.

Each of these DIW extrusion methods is governed by parameters such as temperature, nozzle diameter, extrusion pressure, and movement speed, which must be optimized to achieve the desired outcomes in the final printed structures.

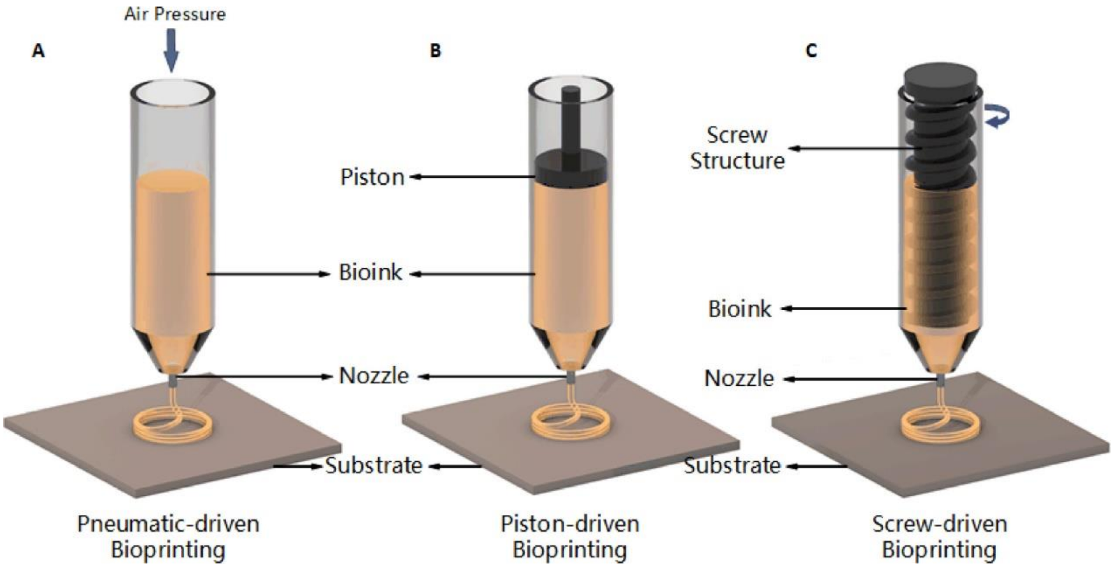

***Figure 2-1** Principles of direct ink writing* [9].

2.1.2 Multimaterial Direct Ink Writing

One significant challenge faced by conventional and many existing additive manufacturing techniques is the simultaneous fabrication of multiple materials within a single geometry while ensuring structural stability and functionality. DIW holds great potential in this area because it enables the combination of various materials and formulations in complex structures, minimizing waste and reducing production time by eliminating component assembly. It also expands the design space, allowing for innovative products, composites, and devices with integrated structural and functional properties. Depending on the method of implementation, multimaterial DIW are categorized into four types: multi-nozzle sequential multimaterial DIW, single-nozzle continuous multimaterial DIW, core-shell co-extrusion DIW and mixing ink DIW [10].

Multi-nozzle sequential multimaterial DIW typically involves printing each material individually with multiple nozzles [11-19]. This method requires precise alignment of each nozzle and meticulous control over starting and stopping the ink flow as needed. Additionally, to ensure a strong interconnection, accurate control of the interface between extruded lines is crucial. Using sequential multimaterial DIW, Blake *et al.* [16] and Wei *et al.* [15] successfully developed fully 3D printed Li-ion batteries (LIB) (Figure 2-2a). They created high-performance, printable Li-ion battery electrolytes, carbon-ceramic composite electrodes and polymers-ceramic composite separator. This approach ensured a tight and continuous interface, crucial for stable discharge voltage in flexible energy storage devices under mechanical stress and the printed LIB exhibited excellent areal capacity. The sequential strategy was employed to fabricate a microsupercapacitor (MSC) by printing vanadium pentoxide and graphene-vanadium nitride quantum dots [18]. This 3D-printed MSC, featuring interdigitated electrodes, exhibited excellent structural integrity, high areal mass loading (3.1 mg/cm^2) and a wide electrochemical potential window (1.6 V). The literature is rich with examples of sequential multimaterial DIW, particularly demonstrating its potential for electrochemical energy storage devices [17], sensors [11, 12] and soft robot [20]. In bioprinting, based on the sequential method, Fang *et al.* [13] developed a strategy called SPIRIT (Sequential Printing In a Reversible Ink Template), which allowed for the creation of complex organ models with intricate vascular networks. The approach successfully printed ventricle models with functional vascular systems, greatly enhancing the precision of bioprinting and offering potential for faster therapeutic tissue and organ fabrication. Moreover, by using multiple nozzles to deposit different bioinks precisely in a single region simultaneously, Gao *et al.* [14] successfully printed thin-walled structures and organ models with strong layer adhesion and minimal contamination. This method enhanced structural precision and integrity.

Single-nozzle continuous multimaterial DIW allows multiple materials extruded through a single nozzle by using microfluidic printheads with the ability of on-the-fly material switching. Hardin *et al.* [1] initially designed and fabricated a specialized microfluidic printhead to seamlessly switch between two viscoelastic inks, enabling the creation of complex 1D, 2D, and 3D architectures with sharp material transitions. Similarly, Liu *et al.* [21] developed a bioprinting platform for fabricating complex, cell-laden structures. The platform integrates seven individually controlled bioink reservoirs connected to a single printhead, allowing simultaneous and seamless switching between bioinks. The team created sophisticated patterns like a heart and kidney using a combination of cell-laden hydrogels. Skylar-Scott *et al.* [2] designed specialized printheads that extend the single nozzle of the printhead to multiple nozzles in the XY direction, allowing it to extrude material at multiple positions simultaneously which significantly improves printing efficiency (Figure 2-2b). To demonstrate its capabilities, the team printed a Miura origami pattern and a millipede-like soft robot by co-printing multiple epoxy and silicone elastomer inks with varying stiffness levels. However, this work is limited to the objects with periodic layouts, since the nozzles cannot be switched independently. The above-mentioned studies were limited to shear-thinning inks (Herschel-Bulkley). By integrating a unique pressure-controlled ink injector system, Hassan *et al.* [22] expanded the capability of such pneumatically driven switching printheads to accommodate more widely and commercially available Newtonian inks.

Core-shell co-extrusion DIW is often performed using concentrically oriented nozzles to dispense coaxial filaments, which allows for the design and printing structures with complex compositions and geometries [23-27]. Mueller *et al.* [23] printed lattices consisting of multicore-shell pillars by creating a variety of printable materials and customized coaxial nozzles (Figure 2-2c). They analyzed the fracture mechanism of core-shell struts featuring a brittle epoxy shell and a flexible epoxy core, finding that an elastomeric interface helped prevent cracks from spreading from shell to core, thereby providing both stiffness and toughness. A similar strategy was employed to develop carbon fiber/ceramic [26] and polymer/ceramic scaffolds [27], each utilizing core-shell struts. The inks, containing carbon fiber and silicon carbide, were co-extruded to create these scaffold structures, combining the beneficial properties of both materials. Moreover, by continuously rotating the nozzle and controlling the angular-to-translational velocity ratio while co-extruding, Larson *et al.* [25] presented a novel rotational multimaterial 3D printing platform that provides subvoxel control over the orientation of helical features in printed filaments. They successfully printed functional artificial muscles made from helical dielectric elastomer actuators and hierarchical lattices incorporating architected helical struts.

Mixing ink DIW allows multiple materials to be printed simultaneously in a single pass through a single nozzle by incorporating a mixing ink device onto the printhead, and the relative flow rate of each ink can be independently and arbitrarily adjusted in time by means of a computer-controlled dispensing. This method offers the advantages of attaining programmable control of local composition and property of the material, thus realizing functionally graded materials (FGMs). Ober *et al.* [28] designed active mixing printheads to homogeneously mix two disparate inks and printed a silicone-based elastomeric ink in which the concentration of a fluorescent pigment is continuously and discretely changed during printing (Figure 2-2d). They also overcame the kinetic challenges of printing chemically reactive materials by separately feeding the resin and curing agent and printed a 3D honeycomb structure with two-part epoxy. To demonstrate the functional advantage, they mixed two inks of highly conductive silver nanoparticle and carbon colloidal inks with varied ratio to continuously control the electrical resistivity of the printed structure. Ren *et al.* [29] fabricated polyurethane parts with diverse gradient patterns and proved that gradient designs significantly reduced stress concentration. By precisely controlling mechanical gradients, Kokkinis *et al.* [30] developed a mixing DIW platform that can produce defect-tolerant materials with customizable failure characteristics. Song *et al.* [19] used mixing

DIW platform to fabricate bilayer structures with active materials that swell in response to water and implemented gradients across the bilayers to control strain mismatch between layers, enabling precise deformation. To overcome the challenge of mixing high viscosity polymer inks in low Reynolds number flows, Hassan *et al.* [31] designed a printhead with a floating static mixer which is capable of dynamically blending silicone-based inks.

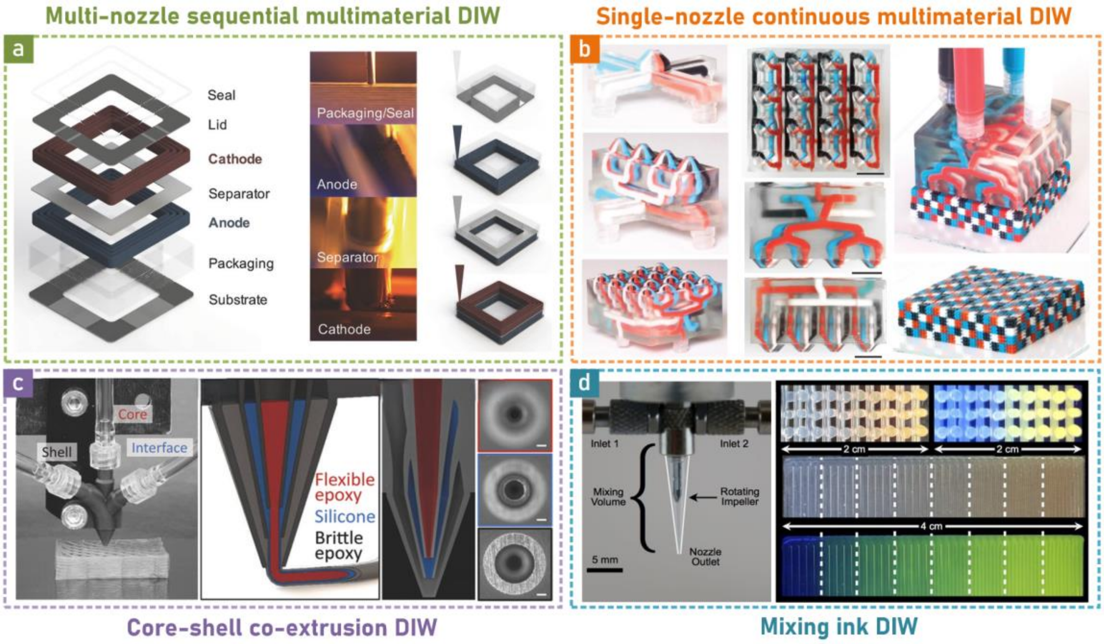

Figure 2-2 *Multimaterial DIW. a) Fully 3D printed and packaged Li-ion battery (LIB) made using multi-nozzle sequential multimaterial DIW* [15]*; b) Photographs of the corresponding 0D, 1D and 2D four-material MM3D printheads; Photographs showing the top and side views of a 4 × 4-nozzle, four-material printhead; Scale bars, 10 mm; Voxelated matter produced by single-nozzle continuous multimaterial DIW* [2]*; c) Photograph of the coaxial printhead connected to the core, interface, and shell ink reservoirs; Schematic cross-sectional view of the C–S printhead* [23]*; d) Photographs of the impeller-based active mixer; Images of the cross-section of a 3D rectangular lattice structure showing continuous change in fluorescent pigment concentration under bright light and UV radiation; Images of a 2D carpet structure showing a discretely varying fluorescent gradient at eight different mixing ratios under*

bright light and UV radiation. Dashed white lines have been added to mark the regions of different mixing ratios [28].

2.2.3 Application of DIW

DIW stands out in the manufacturing field due to its high customizability and the ease with which its setup can be altered using low-cost, interchangeable components such as the three-axis platform, computer, and dispenser. Furthermore, the printing conditions can be adapted by integrating external stimulants like magnetic fields [32], electromagnetic waves [33], acoustic waves [34], and heat sources [35], allowing for the creation of 3D structures with precisely controlled microstructures. This adaptability has spurred extensive research into the 3D printing of various materials including polymers [6, 36, 37], metals [38-40], ceramics [41-43], and biologically active materials [44, 45], each with customizable mechanical, electrical, thermal, chemical, and biological properties. The diverse applications of DIW span from biomedical devices [46] and artificial organs [47] to tissue engineering [48], energy storage [49], optoelectronics [50], metamaterials [51], soft robotics [7], electronics [52], sensors [53], and even food printing [54]. While currently predominantly used for small-scale research and prototyping, DIW has significant potential for the rapid production of industrial-level prototypes. Given its versatility and ongoing advancements, DIW is expected to increasingly influence various industrial sectors in the future.

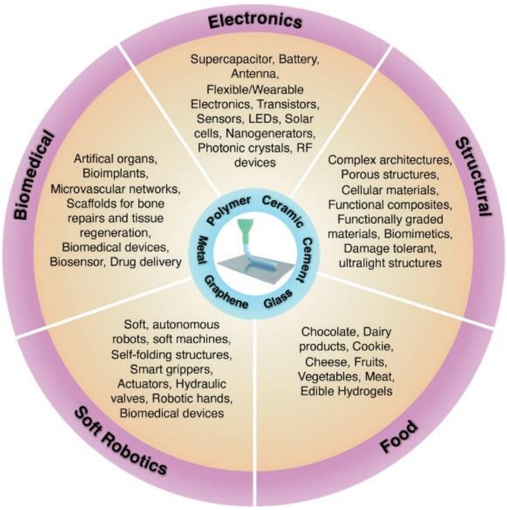

Figure 2-3 *Synopsis of materials used for DIW & their various applications* [10].

In electronics, the flexibility, design freedom, and rapid development capability brought by DIW for micro/nano-scale material printing and/or structure development have found various applications. Eco-friendly formulations for sandwiched [15] and interdigitated [55] full cell printing have been realized (Figure 2-4 a-i), which include highly efficient electrodes of different materials and topologies, and these devices show excellent performance. For flexible electronics, DIW provided possibility for the fabrication of wearable and flexible strain and tactile sensors [12, 56] (Figure 2-4 a-ii) with topological conformity, interwoven 3D geometries, and programmable integration of multiple materials and functionalities. Additionally, DIW has been used to create microelectrodes [57, 58] and electronic contacts / interconnects [59-61]. It can pattern both planar and 3D, as well as reconfigurable interconnects [62] (Figure 2-4 a-iii), on various substrates. This technology is promising for designing circuits in electronics like solar cells, LEDs, transistors, and antennas (Figure 2-4 a-iv) [57, 62-64].

In soft robotics, DIW involving polymeric materials is extensively used in soft robotics, biomedical devices, and actuators [65, 66]. Often, 4D printing [67] aids in developing these devices. Through external stimuli like light [68], magnets [32], or heat [69], specific mechanical and biological [70, 71] movements or deformations can be triggered in these structures (Figure 2-4 b-i,ii) [72].

In structural applications, DIW has emerged as a straightforward, reliable, and eco-friendly production technique capable of crafting new structures with complex architectures [51, 73, 74], layered porosity [42, 75, 76], and functional cellular networks [43, 77]. By incorporating external field control and mechanical movements into the process, it offers enhanced control over the placement of reinforcements [78-80] within the matrix (Figure 2-4 c-ii). This versatility, combined with the capability for multimaterial and multi-nozzle printing, enables the creation of functionally graded materials [30, 81] and structures that are more resistant to damage (Figure 2-4 c-i) [23].

In food printing, DIW has shown great promise in fields like the military, space exploration, and medicine for providing tailored nutrition, design customization, streamlined supply chains, and optimized material use and costs. The technology is particularly beneficial in environments where processing or sourcing materials is difficult, costly, or restricted, such as space missions or for individuals with dysphagia [82, 83]. A wide range of food materials have been successfully printed, including those that are easy to extrude like chocolate, cheese [84], edible hydrogels, cookie dough, and dairy products [85] to more complex materials like fruits [86], vegetables [87], and meats [88] (Figure 2-4d).

In biology and biomedicine, DIW has demonstrated significant potential for broad use in biomedical and tissue engineering due to its ability to print diverse materials. Its printing techniques ensure cell viability, and the room temperature process supports the survival of soft materials like biopolymers [8, 89], cells [90], and bacteria during printing (Figure 2-4 e-i). Key applications include artificial organs and bio-implants [91], microvascular networks [92], bone repair scaffolds [93-96], tissue regeneration [97, 98], (Figure 2-4 e-ii,iii), and biomedical devices [99, 100].

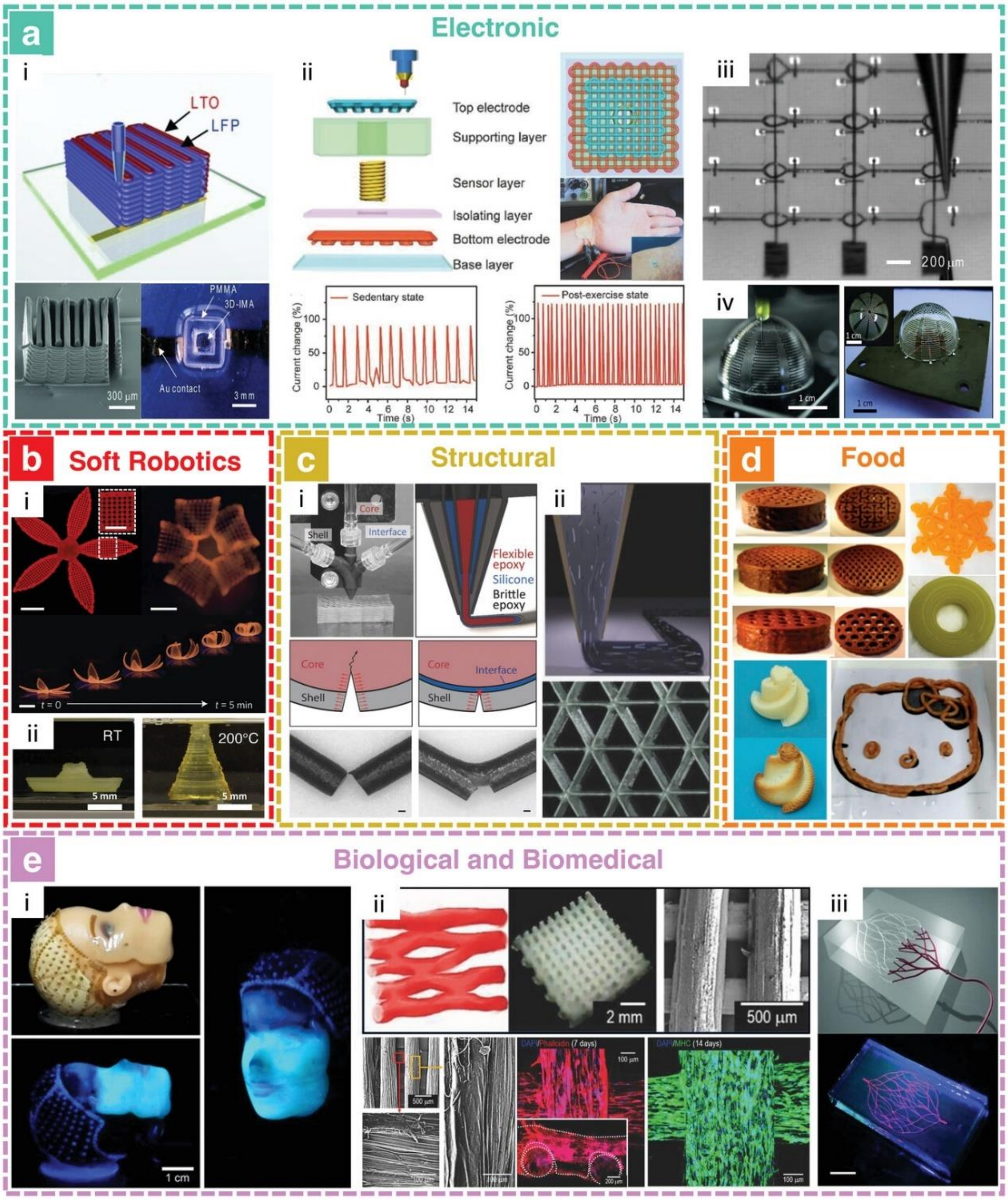

__Figure 2-4__ DIW applications. a-i) Schematic illustration of direct-write assembly of interdigitated micro-battery architecture [55]. (ii) Schematic of the tactile sensor consisting of a base layer, top and bottom electrodes, an isolating layer, a sensor layer, and a supporting layer [101]. (iii) Photograph of silver interconnects on a 4-by-4 LED chip array [102]. (iv) Photograph of a printed antenna [64]. b-i) 90°/0° Flower morphologies generated by biomimetic 4D printing [103]. (ii) Comparison between printed hemitoroidal shell structures at room and 200 °C temperature [104]. c-i) Photograph of the coaxial

printhead connected to the core, interface, and shell ink reservoirs [105]. (ii) Schematic of the progressive alignment of high aspect ratio fillers within the nozzle and triangular honeycomb structures composed of SiC-filled epoxy [37]. d) Chocolate with plant sterol powder and different infill patterns [106]; cookie dough (with xanthan gum) before and after baking [107]; vitamin-D enriched orange concentrate with wheat starch and k-carrageenan; printed lemon juice gel in ring shape; meat. e-i) A doll face is scanned and coated with a 4.5 wt% Flink solution. (ii) Schematic of cardiac and muscle structure, and images of aligned microfibers in a polycaprolactone mesh and cellular alignment in a cultured environment [97]. (iii) Images of 3D-printed microvascular networks showing the intricate network channels and their fluorescent imaging [92].

2.3 3D Food Printing

2.3.1 Background

3D food printing (3DFP) leverages advanced techniques such as extrusion, selective laser sintering, and inkjet printing to convert a wide range of food materials into customizable and intricate edible products. This method enables the creation of food items that can be finely tuned for nutritional content, texture, and appearance that were previously difficult or impossible to achieve with traditional food processing techniques, appealing significantly in culinary, healthcare, and food manufacturing industries.

In healthcare, 3DFP caters to specific dietary needs by adjusting food composition for individuals with unique health requirements or preferences, which could revolutionize diet planning in clinical settings for patients with specific dietary restrictions. In culinary, 3DFP enhances the dining experience by allowing chefs to innovate with complex food designs and textures that are difficult or impractical to achieve with conventional cooking techniques. This has the potential to transform premium culinary presentations, providing a novel dining experience. In food manufacturing industries, 3DFP enables the efficient production of customized food shapes and textures, potentially reducing waste and optimizing ingredient use. The ability to produce food on-demand in varied forms without the need for traditional molds or tools can lead to significant reductions in production costs and material waste, which is crucial for sustainability in food production.

The extrusion method is favored in 3D food printing due to its ability to shape fresh foods, which are typically in paste or liquid form, into desired forms by extruding them through printer nozzles. Specifically, the method is adaptable for various food materials, including semi-solid or viscous substances. For instance, it's suitable for materials that require temperature control to maintain the right viscosity for extrusion, such as chocolate, which needs to be maintained within specific temperature ranges.

2.3.2 Multimaterial Food Printing

Coaxial nozzle extrusion is a technology where a coaxial nozzle that simultaneously extrudes two or more materials concentrically along a common longitudinal axis, using multilayer nozzles [108]. In food printing, coaxial extrusion enables the layering of multiple ingredients through varied combinations, allowing for the creation of complex and redesigned products with enhanced appearances and interesting shapes. Kim *et al.* [109] used a coaxial 3D printing system to apply potato starch solution as a shell around a surimi core, mimicking the structure of crab meat. The study found that a 12% potato starch solution provided the best cooking performance, water retention, and printing characteristics. The 3D printed surimi-based crab meat, with its linear patterns, compared favorably to commercial alternatives. Vancauwenberghe *et al.* [110] demonstrated 3D printing of pectin-based food using coaxial printheads. The inner flow consisted of low methoxylated pectin with CaCl2·2H2O, and the outer flow was a CaCl2 crosslink solution. Coaxial extrusion offered finer control over the gelation and texture of pectin objects and produced smaller volumes compared to simple extrusion. Ko *et al.* [111] used a coaxial nozzle to incorporate hydrocolloid fibers into a protein matrix, enhancing the texture of meat substitutes (Figure 2-5B). The inner fluid, a mix of ionic hydrocolloids (sodium alginate, carrageenan, glucomannan), flowed through an injection pump, while the outer fluid, a soy protein paste with calcium and potassium ions, was extruded through a 3D food printer. This method improved shape retention and cooking stability by forming an irreversible gel with elasticity similar to beef.

Coaxial extrusion can also be employed to create modified foods that are soft, easy to chew and swallow, ensuring that the elderly receive adequate protein, nutrients, and calories. Chao *et al.* [108] combined chicken surimi with mealworm protein isolate to produce soft and modified surimi as a new diet for the aged population. Similarly, Kim *et al.* [112] incorporated a carrageenan-based protein replacement solution into surimi to produce low-calorie surimi (Figure 2-5A). To obtain more attractive bakery products, Uribe-Wandurraga *et al.* [113] improved the sensory properties of microalgae-rich foods using a coaxial extrusion nozzle to encase a microalgae-enhanced batter inside a standard batter, effectively concealing the green color and making the snacks more appealing to consumers (Figure 2-5D). To improve the nutritional value and meet the consumer needs, Jeon *et al.* [114] developed a curcumin-filled gel using nanoemulsion technology as a nutrient carrier for 3D printing (Figure 2-5C). This approach enhanced curcumin's bioavailability through encapsulation and introduced nanotechnology into custom food manufacturing, allowing for precise inclusion of functional materials.

Coaxial nozzle-assisted 3D printing, capable of creating a core inner layer and a sheath outer layer, is an innovative method for producing tubular structured foods or incorporating functional substances into foods. This technique allows for the simultaneous printing of two different food materials, enhancing shape fidelity, structural complexity, printability, and biocompatibility. Coaxial printing offers significant potential for enhancing the biological activity and mechanical properties of foods, making it highly beneficial for producing nutrient-rich, high-value food products.

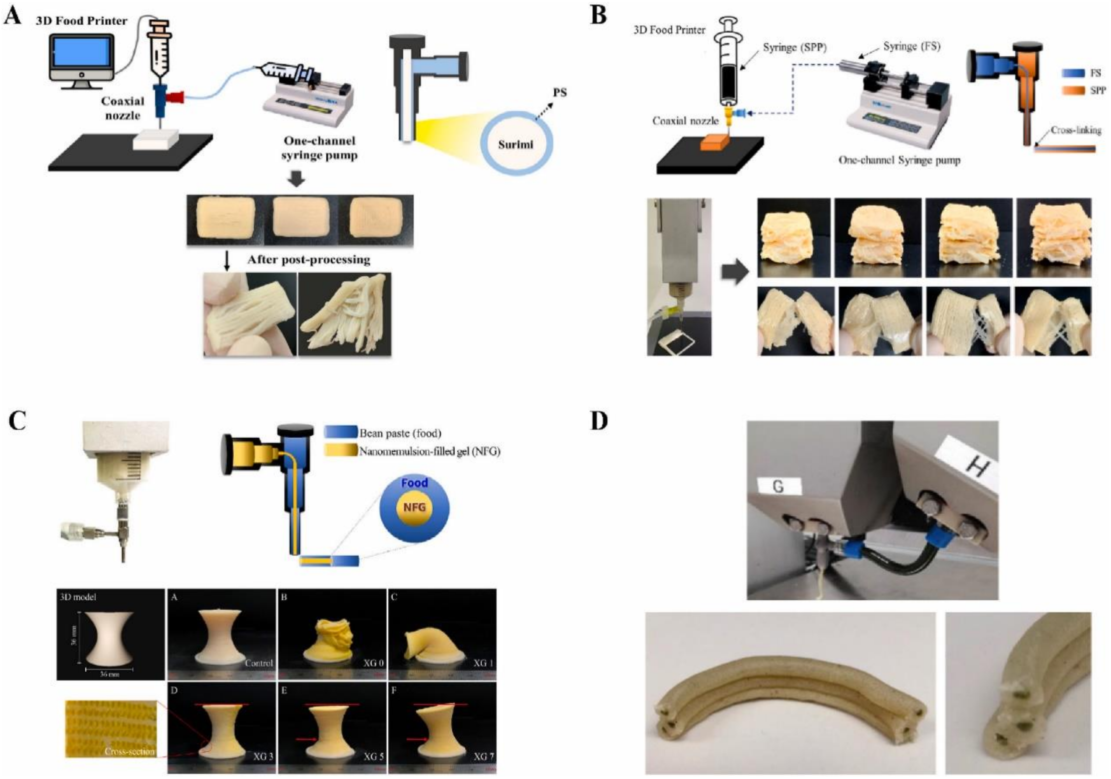

Figure 2-5 *Coaxial nozzle extrusion. A) The surimi-based imitation crab meat* [109]*; B) artificial meat* [111]*; C) customized food produced by nanoemulsion* [114]*; D) snacks rich in microalgae* [113]*.*

Multiple nozzles extrusion is a method using multiple nozzles for continuous alternating printing, capable of simultaneously depositing various inks with minimal cross-contamination, which is the most popular method of multimaterial additive manufacturing [115].

To gain consumer acceptance, 3D-printed food must not only follow specific recipes but also exhibit high geometric complexity and appealing aesthetics. Lipton et al. [116] used a dual-syringe Fab@Home model 2 printer to craft a complex cookie featuring a butter-based outer batter and a 'C' shaped cocoa batter interior, maintaining its form during baking and offering distinct visual and taste qualities (Figure 2-6A). Karyappa and Hashimoto [117] developed two different chocolate-based inks with varying rheological properties for printing a 3D conical structure, where the inner shell contained liquid chocolate syrup, visible upon cutting the shell (Figure 2-6B). Lee et al. [85] utilized a printer with dual syringes for layering chocolate and milk inks, creating structures filled with various syrups like maple, milk cream, chocolate, and blueberry (Figure 2-6C). Additionally, Liu et al. [118] used a double-extrusion printer to create dishes from mashed potatoes and strawberry juice gel, achieving controlled material deposition and producing food with multiple flavors and textures (Figure 2-6D).

Food 4D printing utilizes specific formulations to create printing inks that undergo predictable changes in performance—such as shape, texture, flavor, and color—when exposed to stimuli like water, pH, or temperature [119]. Ghazal, et al. [120] developed inks using red cabbage juice, vanillin powder, and potato starch gel (RCJ-V-PS-G, upper part) alongside a fruit juice gel (apple, orange, lemon, bottom part). Due to differing pH levels, the diffusion of hydrogen ions triggered a reversible transformation in the anthocyanin structures within the RCJ-V-PS-G, causing the print color to shift from blue to shades of purple or red (Figure 2-6F). He et al. [121] explored multi-material printing using purple mashed potatoes and regular mashed potatoes (Figure 2-6G). The interaction between the anthocyanin-rich purple potatoes and potatoes of varying pH levels led to a gradient of color changes due to anthocyanin diffusion. Furthermore, Chen et al. [122] printed an alkaline lotus root powder-curcumin gel system using a curcumin emulsion and microwave stimulation to trigger changes (Figure 2-6H). Shi et al. [123] created a dual-material model consisting of purple potato puree and a beeswax-based oleogel, producing a 4D printed food that automatically deforms under microwave heating (Figure 2-6I).

In China, stuffed foods typically consist of a starch-based or grain-based outer crust filled with various fillings, vegetable oil, and seasonings. This category includes traditional foods like dumplings, steamed buns, pies, vegetable balls, spring rolls, wontons, bean paste buns, Qingtuan, mooncakes, and pastries. Wang et al. [124] employed a dual-nozzle 3D printer to create mooncakes designed for easy swallowing (Figure 2-6J). Similarly, Kong et al. [125] used a dual-nozzle 3D printer to produce Qingtuan suitable for individuals with dysphagia (Figure 2-6K).

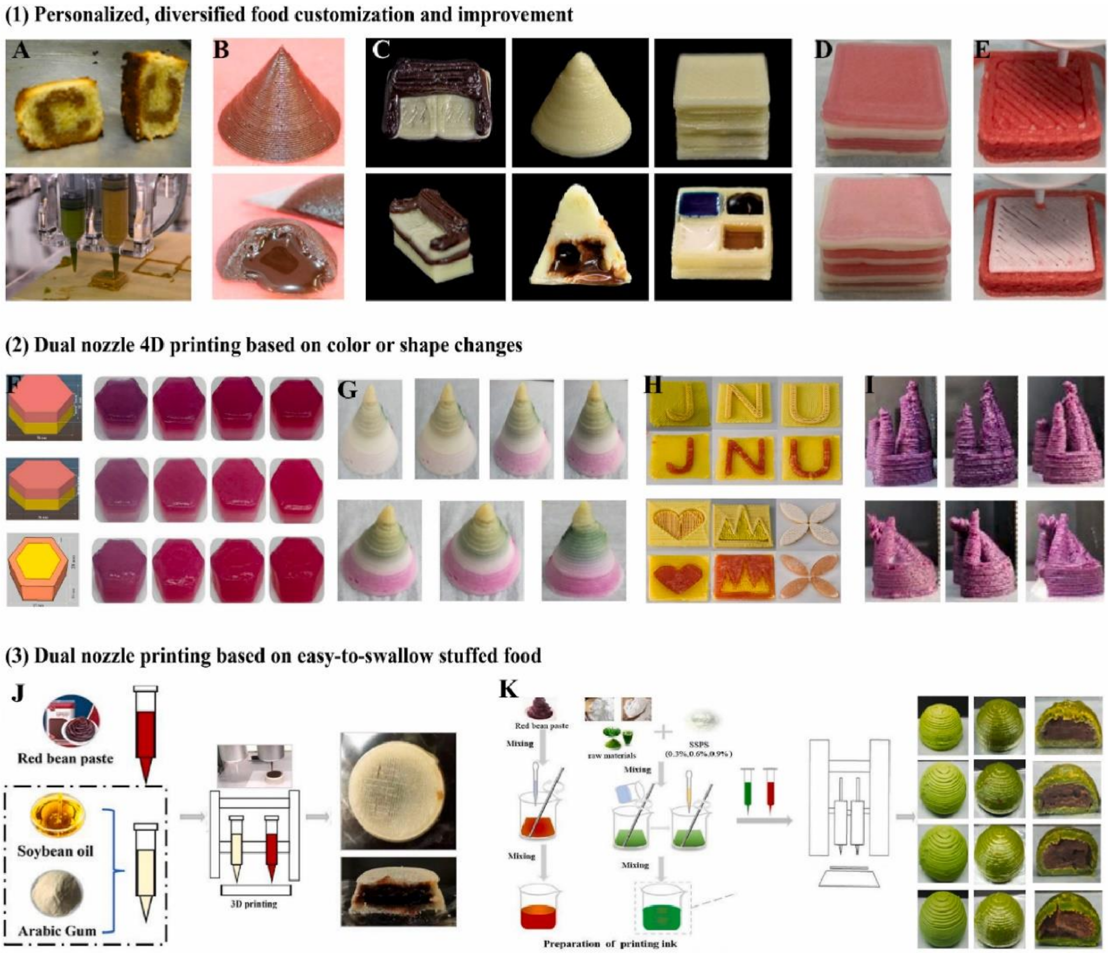

Figure 2-6 *A) Cookie with and embedded extruded C shaped and double-nozzle printed celery turkey cube structure [113]; B) Liquid chocolate-based ingredients [113]; C) Milk and chocolate and other ingredients [85]; D) Mashed potatoes/strawberry juice gel [118]; E) 3D printed composite multi-layer meat; F) RCJ-V-PS and lemon juice gel; G) Mashed potatoes/purple sweet potato puree [121]; H) lotus root powder gel [122]; I) Purple potato puree/oleogel [123]; J) Mooncakes with filling [124]; K) Qingtuan [125].*

2.4 Research Gap

In summary, DIW (Direct Ink Writing) has developed rapidly over the past two decades and has systematic research in multi-material printing. Moreover, DIW has incomparable advantages in food printing, and current research trends are also moving towards multi-material food printing. However, existing multi-material food printing techniques typically use multiple nozzles to print different materials or co-axial extrusion to achieve core-shell structures, which have disadvantages such as low material switching efficiency and high equipment maintenance costs. A single-nozzle multimaterial DIW method has been proposed, it has been validated in various fields and demonstrated advantages such as high switching efficiency, high printing precision, and low equipment maintenance costs, but no studies have yet applied this method to food printing. To address this gap, we applied single-nozzle based method into 3D food printing.

Chapter 3 Methodology

The detailed composition of this method is shown in Figure 3-1, including mechatronics design (section 3.1), materials used in printing (section 3.2) and slicing algorithm (section 3.3). And section 3.4 discusses the challenges and presents the optimization model for improving printing fidelity. This chapter illustrates the final implemented for single nozzle based multimaterial DIW in this thesis.

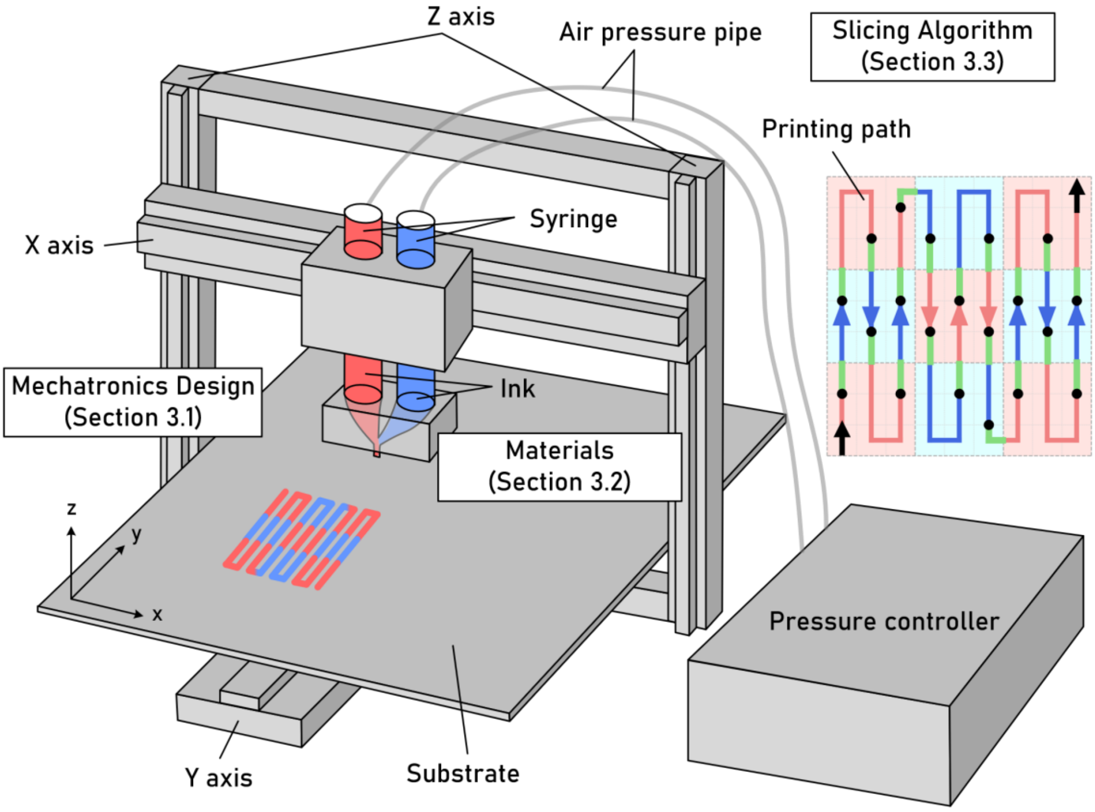

Figure 3-1 Schematic of the printer and methodology.

3.1 Mechatronics design

The mechatronic design encompasses several key components: the motion platform, pneumatic system, control system, printhead and nozzles (Figure 3-2). This multifaceted approach integrates mechanical and electronic elements to achieve precise control and functionality in the 3D printing process.

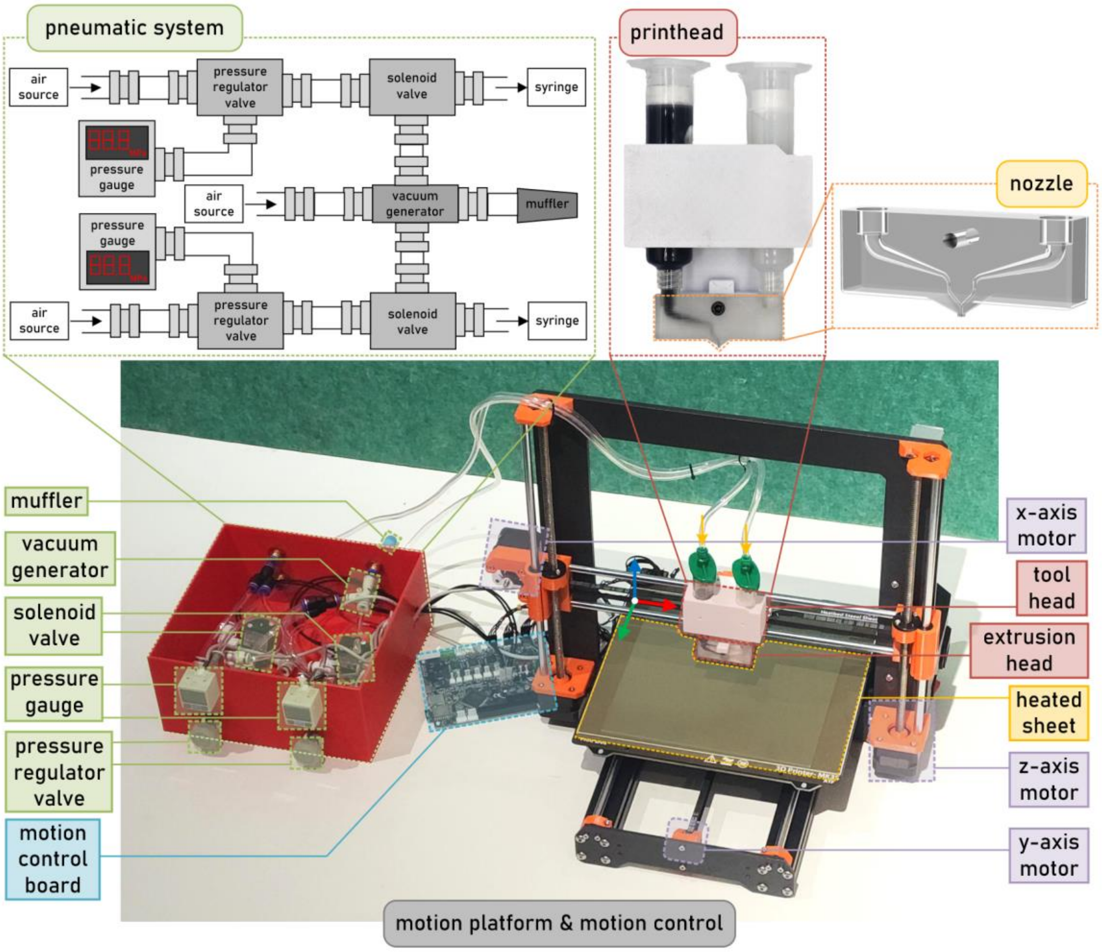

Figure 3-2 Photograph of the printer and schematic of the pneumatic system.

3.1.1 Motion platform

The design of the motion platform primarily focuses on essential factors such as the range of motion, motion accuracy, movement speed, and stability. The Prusa MK3S+ has been selected due to its superior capabilities in handling the demands of DIW 3D printing. This platform offers an XYZ three-axis movement system, which is essential for precise material deposition. It has a maximum build volume of 250 mm x 210 mm x 210 mm, which provides ample space for a variety of printing tasks. Precision is a critical aspect of the platform, with the ability to achieve accuracies up to 0.05 mm. This high precision is coupled with the capacity for rapid movements, reaching speeds up to 200 mm/s, thus striking a balance between speed and fidelity of prints.

The design of the Prusa MK3S+ emphasizes stability and robustness, featuring a dual stepper motor configuration on the Z-axis. This setup enhances both the reliability and ease of use of the printer, making it well-suited for extensive and continuous operation. Moreover, the printer includes a user-friendly leveling design, simplifying the calibration process to ensure optimal printing conditions. The open-source nature of the Prusa MK3S+ further aligns with our project requirements, as it allows for easy modifications and adaptations, particularly with the integration of a custom extruder setup for DIW printing. These modifications are minimal, thereby significantly simplifying the project and reducing setup time.

3.1.2 Pneumatic system

The pneumatic system is designed to fulfill the specific requirements of independently controlling the high-frequency opening and closing of two solenoid valves and setting the air pressure for each valve individually. This system comprises two air regulators (SMC IR1020-01), two pressure gauges (SMC ISE30A-01-N), and two solenoid valves (MAC 35A-ACA-DDAA-1BA). Additionally, it includes a vacuum generator (SMC ZH05DL-06-06-06), a muffler, air hoses, and several quick connectors to facilitate rapid assembly and disassembly. Compressed air flows from the air source into the regulators, where the air pressure is adjusted to meet the specific requirements of the printing process. The adjusted air then passes through the solenoid valves to the pressure gauges, which monitor and display the output pressure, ensuring that it remains within the desired range. The vacuum generator plays a crucial role by utilizing high-speed airflow to create a low-pressure area, enhancing the precision of material handling. This setup allows for the air flow to be directed either towards the syringe for material extrusion when the solenoid valves are open, or towards the vacuum generator for immediate cessation of material flow when the valves are closed, effectively preventing excess material from dripping—similar to filament retraction in FDM printing.

3.1.3 Control system

G-code was chosen as the control code for this study for the following reasons: Firstly, as an industry standard, G-code’s ubiquity and standardization mean it enjoys widespread support, allowing users to leverage a wealth of resources, tools, and community support; Secondly, G-code allows for precise control over every detail of machine movement, including speed and position, which is crucial for this study. Additionally, the flexibility and programmability of G-code enable users to write or modify code to suit specialized needs or complex projects, offering high customization. Due to G-code’s compatibility benefits, users can easily transfer codes between different brands and types of machines, enhancing usability.

To meet the requirements of a control system capable of executing universal G-code and managing four stepper motors and two solenoid valves for multi-material DIW 3D printing, the Duet2 WIFI board was selected. This board, integrated with RepRapFirmware, offers wireless connectivity that simplifies the transmission of motion paths from PC to printer. Its Trinamic TMC2660 stepper drivers enhance precision and reliability by supporting sensorless homing, which eliminates the need for mechanical limit switches. And the board’s fan outputs could be configured as GpOut pins to control solenoid valves. The user-friendly, non-compile configuration simplifies printer setup and management, minimizing the need for modifications and enhancing printer performance, thereby providing an efficient control solution for this study.

3.1.4 Printhead and nozzle

The design of the printhead and nozzle was carried out using Autodesk Fusion360, specifically engineered to attach to the end-effector of an XYZ motion platform. This printhead configuration allows for the mounting of two syringes and integrates seamlessly with Prusa MK3S+ standard printhead mounting points. Each printhead is equipped with two vertical circular holes, sized to accommodate the widest point of the syringes, ensuring a secure fit. For the nozzle, the design includes a circular hole at the bottom of the printhead, alongside a space for securing a nut to facilitate easy nozzle attachment. A positioning block was integrated to maintain the nozzle alignment parallel to the XY plane, crucial for consistent material deposition. The printhead was then produced using Fused Deposition Modeling (FDM) 3D printing technology. Regarding the syringe setup, standard disposable syringes equipped with air tube adapters were employed, typical of those used in dispensing machines. It is vital to install a piston post-filling to achieve even pressure distribution within the syringe, preventing uneven force application and air entrapment during material extrusion. The nozzle's design includes threaded connections to the syringe, allowing a smooth transition in the flow channel from the syringe's opening diameter down to the nozzle's exit diameter. This gradual transition is maintained until the materials' flow paths converge, minimizing turbulence and ensuring airtight connections. The internal flow channels are designed to be as smooth as possible. For this study, nozzle diameters of 0.7, 0.8, 0.9, and 1.0 mm were selected, with the nozzles themselves produced using Digital Light Processing (DLP) 3D printing to achieve the required precision. Although transparent resin was initially chosen to visually monitor the material flow within the channels, grey resin was ultimately used for the final tests due to its superior printing accuracy.

3.2 Materials

In this study, the work on materials involved selecting appropriate materials, developing formulations, measuring rheological properties, and testing printing parameters.

3.2.1 Material preparation

The material should behave as a non-Newtonian fluid and exhibit shear thinning properties, meaning it becomes less viscous under shear stress, which needs to be low enough to be extruded through the nozzle but quickly regains high viscosity to hold its shape upon deposition.

Regarding the material used for printing test, we initially chose face cream (NEVIA) due to its shear-thinning properties and suitable semi-solid-like viscosity. However, since it was difficult to be filled into the syringes without air bubbles, we finally chose Vaseline, which could be heated to a liquid and easily filled into the syringes without air bubbles (Figure 3-3).

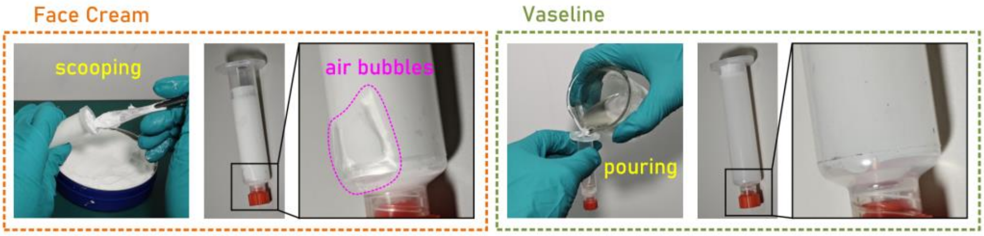

Figure 3-3 Comparison between face cream and Vaseline.

White Vaseline Preparation: Take milky white, semi-transparent Vaseline (HYNAUT white Vaseline) and place it in a beaker. Heat it to 90°C until it becomes clear and fluid. The Vaseline is then ready to be transferred directly into a syringe. After inserting the plunger, invert the syringe and allow it to cool to ensure that no air bubbles are present inside. (Figure 3-4)

Black Vaseline Preparation: To visually differentiate and change the viscosity of the material, black Vaseline could be prepared by adding carbon powder to the heated and transparent Vaseline at a concentration of 5% w/v (i.e., weight per volume ratio; e.g., 5g carbon powder per 100ml Vaseline). Stir the mixture thoroughly and transfer it into a syringe as described above. The diameter of the carbon powder used in the experiment ranges 5-15 μm, and it is filtered through a sieve to remove clumps.

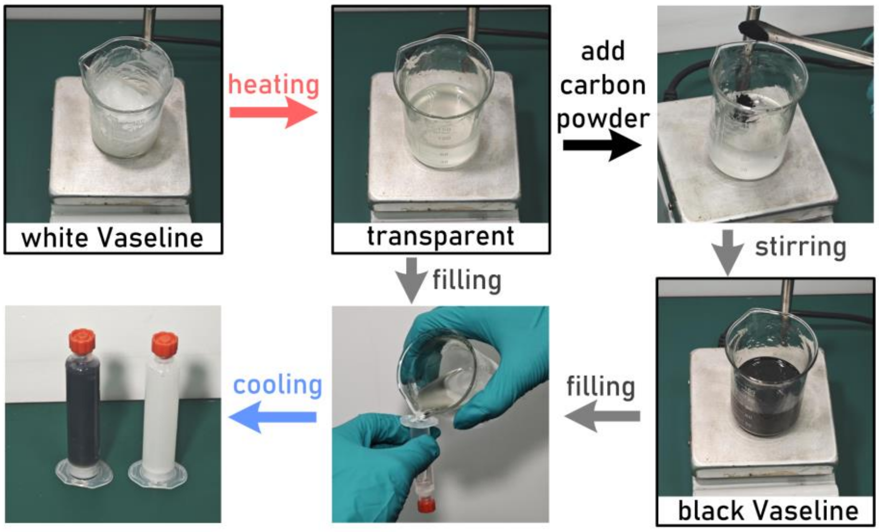

Figure 3-4 Preparation of Vaseline.

Regarding the material used for 3D food printing, we developed several extrudable edible formulations.

Mashed Potatoes: Prepare mashed potatoes by mixing potato powder (Jiangsu Runhui Food Co., Ltd.) with distill water in a 1:1.2 volume ratio.

Salted mashed potatoes: Add salt (Xuetao Refined Iodine-Free Sea Salt) at a concentration of 1% w/w and mix evenly. Orange PCB pigment (Qingdao Qianzi Biotechnology Co., Ltd.) is added to the salted mashed potatoes at a concentration of 0.01% w/w.

Ketchup: the printable ketchup was prepared by mixing the commercial one (Heinz (Qingdao) Food Co., Ltd.) with 20 w/v% gelatin solution. The gelatin (Yuanlong Food Ingredients Co., Ltd.) solution was prepared by mixing 5g into 100g distill water and stirred at 50°C until it is fully dissolved.

3.2.2 Rheological characterization

We used a rotational rheometer (Malvern KNX2100) with a parallel plate (PU40 SR1133 SS) to measure the rheological properties. The experiments were performed at a controlled temperature of 25°C. The gap between the plates was set at 1mm. The shear rate was varied from an initial rate of $10s^{-1}$

up to 500 s^{-1}, with ten data points recorded at each decade. All rheological measurements were performed in triplicate. The data on the shear stress versus shear rate were fitted using Python to the Herschel-Bulkley model, which describes the rheological behavior of non-Newtonian fluids. This fitting process allowed us to plot viscosity as a function of shear rate (Figure 3-5).

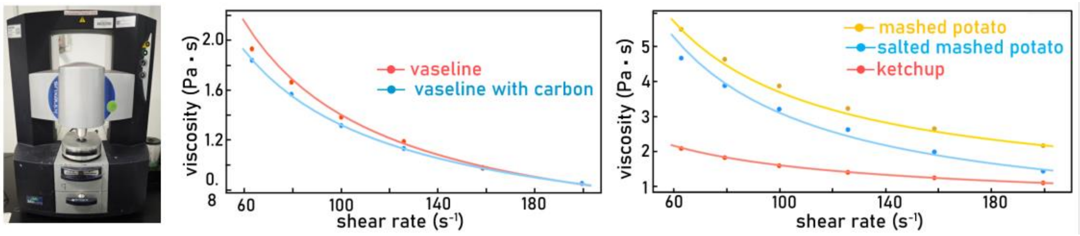

Figure 3-5 Photograph of rotational rheometer and graphs of viscosity.

3.2.3 Printing parameter

The flow rate is adjusted by controlling air pressure based on the desired layer height and printing speed. Consequently, it’s critical to calibrate the air pressure to avoid excessive force that could disrupt the material’s integrity or too little force that could lead to inadequate extrusion. In particular, pressure drop occurs during the flow of printing materials, so it must be considered. For the regular shaped channels, the pressure drop could be calculated, which is related to the cross-sectional area and length. However, the cross-sectional area of the exclusive channels and the syringe is constantly changing, making it difficult to calculate. Thus, we measured the pressure at the outlet of the exclusive channels, that is, the pressure on the fluids of the shared channel (Figure 3-6). And the pressure drop of the shared channel could be calculated due to the regular shape.

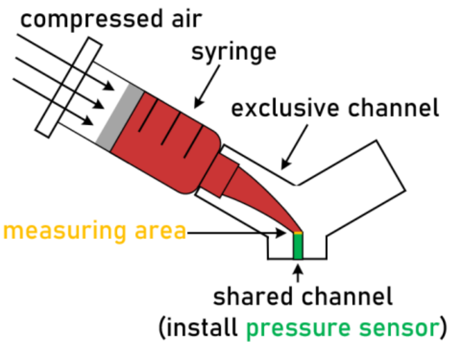

Figure 3-6 Schematic of measuring pressure.

3.3 Slicing algorithm

Since none of the existing slicing software support single-nozzle based multimaterial DIW which could switch materials on-the-fly, we developed a slicing algorithm that support on-the-fly material switching and could integrate our proposed optimization. Specifically, it divided into two parts: preprocessing and path generation.

3.3.1 Preprocessing

The printing object is usually saved as a 3D model or 2D image, which needs to be converted into a two- or three-dimensional array of material type of the corresponding position. For 3D models in assembly format (typically .step files), this involves exporting each material component in STL format, recording the minimum coordinates in each axis of the assembly's coordinate system (Figure 3-7a1), voxelizing the model using a ray-casting algorithm, assigning material types to voxels (Figure 3-7a2), and arranging the model into a three-dimensional array for layer-by-layer export (Figure 3-7a3). For 2D images in formats like .jpg, .png, or .bmp, we perform resizing via Bilinear Interpolation Algorithm, followed by binarization to map the image to a bitmap format based on predefined thresholds (Figure 3-7b2). In cases of multiple materials, additional rules map types by setting diverse threshold ranges and adjusting RGB values for pixels within those ranges while enhancing visualization. Next, we align the coordinate systems between the printing system and the imported data, which may require rotation or flipping (Figure 3-7c).

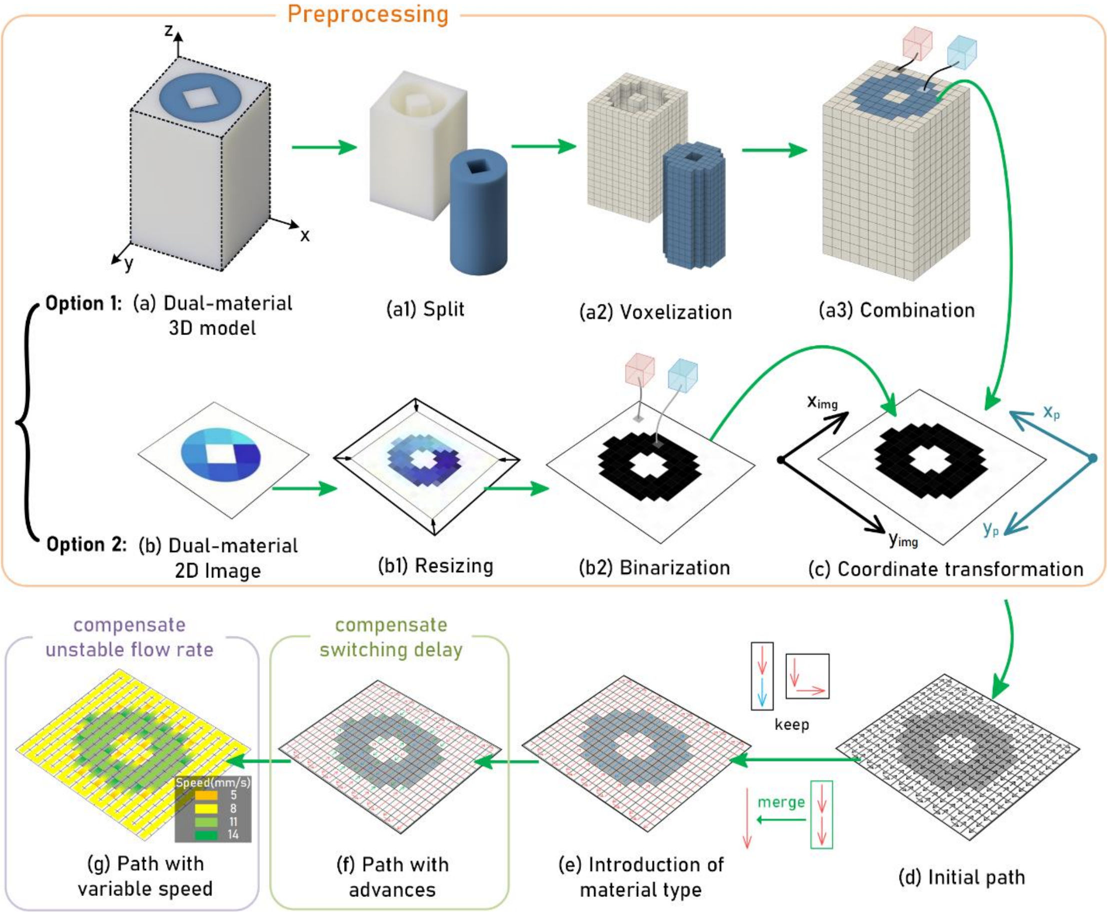

Figure 3-7. Flowchart of Path Generation. a) *Process of importing dual-material 3D model;* ***b)*** *Process of importing dual-material 2D image.* ***c)*** *Transformation from coordinate system* $(x,y)_{img}$ *to* $(x,y)_{printer}$*;* ***d)*** *Schematic of initial path;* ***e)*** *Introduction of material type, different colors correspond to different materials;* ***f)*** *Path with advanced switching points, green path indicates switching in advance;* ***g)*** *Speed heatmap with adaptive movement speed.*

3.3.2 Path generation

An initial path is generated to traverse the entire 2D array (Figure 3-7d), with material types assigned to the correlated path for printing. Adjacent paths with the same direction and material type are merged for computational efficiency (Figure 3-7e).

Next, switching points are advanced based on the calculated distance (Figure

3-7f), and corresponding speeds are assigned to paths within a certain distance before these points (Figure 3-7g). This comprehensive slicing strategy addresses the challenges of integrating complex 3D models and 2D images, enabling real-time material switching during printing with a focus on high-precision results.

In the stage of implementation, we detail the practical code flow for our algorithm (Figure 3-8). Initially, we define critical variables and functions for path generation. The array $Pa[]$ stores paths with attributes like start and end points, material type, and direction. adv_d denotes the advance distance for material switching, and $dis(point\_1, point\_2)$ measure distances between points.

Data processing unfolds in four primary steps:

Generate initial paths and switching points: We select a start point and set the traversal direction based on its position. Paths are generated by checking adjacent points and material types, creating a path array $Pa[]$ with respective material types for each segment.

Advance switching points: Here, we sequentially traverse $Pa[]$, adjusting the end points of paths at material switching points based on the remaining advance distance calculated from adv_d.

Simplify paths: This step involves merging adjacent paths with identical material types and movement directions, enhancing computational efficiency.

Set movement speed and export G-code: We traverse $Pa[]$, splitting paths into segments near switching points and calculating movement speeds for each segment based on our model. This data is then formatted into G-code for printing. This comprehensive process ensures precise material switching, addressing challenges in single-nozzle MM-DIW printing.

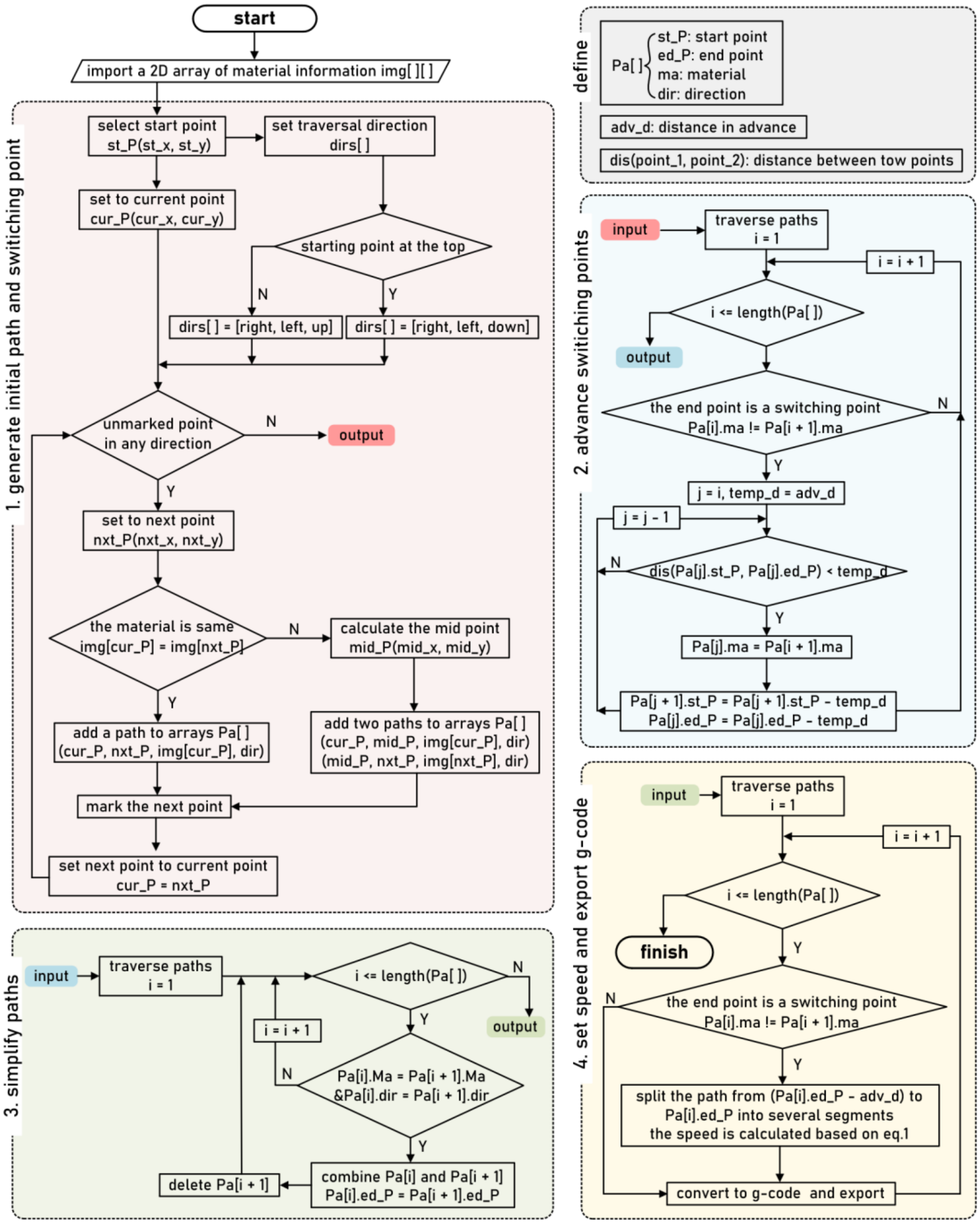

Figure 3-8 Flowchart of the Code Process: *(1) Flowchart for generating initial path and switching point; (2) Flowchart for advanced switch points; (3) Flowchart for simplifying the path; (4) Flowchart for setting speed and exporting G-code.*

3.4 Optimization model

3.4.1 Delay compensation

As previously mentioned in section 1.1, residual material in the shared channel when switching materials can cause extrusion delays, preventing the target material from being deposited accurately at the planned positions. This issue is particularly noticeable when printing small-sized multimaterial features, where frequent and accurate material switching is necessary. To mitigate this, we propose a path planning model that compensates for this delay, ensuring accurate material placement.

The advance distance L_{adv} can be calculated by Eq. (1) because the segments Q_1 and Q_2 have the equal volumes during material switch (Figure 3-9),

$$L_{adv} \cdot S = \frac{\pi d^2 (L_s + H)}{4}, \tag{1}$$

where d is the nozzle diameter, L_s is the shared channel length, S is the cross-sectional area of the deposited materials, and H is the length of extruded yet undeposited material.

Considering the hanging material results in material deposition delay when the nozzle height h_2 is greater than the print height h_1, the length H can be calculated by Eq. (2).

$$H = max(h_2 - h_1, 0) \tag{2}$$

The cross-sectional area S in Eq. (1) can be calculated by

$$S = \frac{Q}{v}. \tag{3}$$

where v is the printhead movement speed, and Q is the extrusion flow rate and can be calculated based on *Poiseuille's law* [126] as Eq. (4)

$$Q = \frac{\pi d^4 P}{128 \mu L_s}, \qquad (4)$$

where P is the driven pressure on the material inside shared channel, and μ is the material viscosity.

Note that (i) the extrusion material was considered as Newtonian fluids because the shear rate during the extrusion printing process remains ca. 104±8 s^{-1} and the material viscosity has only 6% deviation (see details in the supplementary information), and (ii) the pressure on the material inside shared channel P can be experimentally measured.

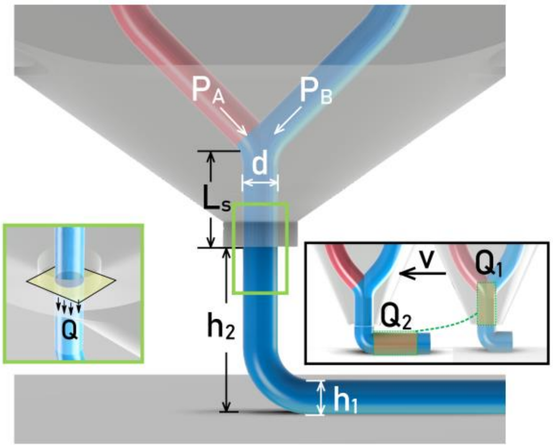

Figure 3-9 Schematics of the nozzle outlet with the relevant dimensions labeled.

3.4.2 Extrusion compensation

The over-extrusion-induced bulging occurs when switching from a low- to high-viscosity material due to the residual material in the shared channel, while the under-extrusion-induced necking in the reverse scenario. An idea solution can be a pneumatic system capable of real-time adjusting extrusion pressure but with costly hardware. The more practical solution is to fix extrusion pressure while adaptively control the printhead speed v.

The cross section area of the print (symbolized by S) should be a fixed value so as to keep the printing fidelity. Therefore the time-dependent printhead speed $v(t)$ is directly proportional to the instantaneous flow rate $Q(t)$ as Eq. (5)

$$v(t) = \frac{Q(t)}{S}. \tag{5}$$

Based on *Poiseuille's law* [126], the instantaneous flow rate $Q(t)$ can be calculated by Eq. (6)

$$Q(t) = \frac{\pi \cdot d^4}{128[\mu_{cur} \cdot L_s \cdot \phi_{cur}(t) + \mu_{nxt} \cdot L_s \cdot \phi_{nxt}(t)]} \cdot P_{nxt}, \tag{6}$$

where $\mu_{cur,nxt}$ and $\phi_{cur,nxt}(t)$ are separately the viscosities and the instantaneous volume percentages of the current and the next material, and P_{nxt} is the driven pressure of the next material.

The instantaneous volume percentages $\phi_{cur,nxt}(t)$ in Eq. (6) is related with the extruded material volume $V_{ext}(t)$ as Eq. (7)

$$V_{ext}(t) = \frac{\pi d^2}{4} \cdot L_s \cdot \phi_{nxt}(t). \tag{7}$$

Based on the physical definition, the instantaneous volume $V_{ext}(t)$ can also be obtained by integrating the flow rate $Q(t)$ from zero (referring to the starting point) to a certain material switch moment t as Eq. (8)

$$V_{ext}(t) = \int_0^t Q(t) \cdot dt \ , \ \ t \in [0, t_0], \tag{8}$$

where the maximum material switch period t_0 can be calculated as Eq. (9)

$$t_0 = \frac{(a \cdot V_s + b)^2 - b}{2a}, \tag{9}$$

where $V_s = \frac{\pi d^2 L_s}{4}$ is the volume of the shared channel, and the two the variables a and b are separately

$$a = \frac{512 \cdot (\mu_{nxt} - \mu_{cur})}{\pi^2 d^6 \cdot P_{nxt}}, \tag{10}$$

$$b = \frac{128 \cdot \mu_{cur} \cdot L_s}{\pi d^4 \cdot P_{nxt}}. \tag{11}$$

By combining Eqs. (6-8), the time-dependent flow rate $Q(t)$ can be

$$Q(t) = \frac{1}{\sqrt{2a \cdot t + b^2}}. \tag{12}$$

Considering the standard G-code based numerical systems control motions via discrete movement speed for each command line, the equivalent average material extrusion flow rate $\bar{Q}(t)$ for a discrete step can be expressed as

$$\bar{Q}(t) = \frac{\int_t^{t+\Delta t} Q(t) \cdot dt}{\Delta t}, \tag{13}$$

where Δt is the timestep for each discrete control cycle.

Therefore, the final time-dependent printhead speed $\bar{v}(t)$ adaptive to different material viscosities used in each discrete numerical control cycle can be

$$\bar{v}(t) = \frac{1}{a \cdot S \cdot \Delta t}\left(\sqrt{2a \cdot (t + \Delta t) + b^2} - \sqrt{2a \cdot t + b^2}\right). \tag{14}$$

Chapter 4 Result & Discussion

4.1 Optimization

4.1.1 Delay compensation

To validate the above model, we conducted a series of experiments using two colored inks to investigate the improvement effect of advance distance on extrusion delay when using different nozzle heights (0.3, 0.6, 0.9, 1.2mm) and diameters (0.6, 0.7, 0.8, 0.9mm) (Figure 4-1a). The theoretical deposition delay values (the distance between the switching and deposition points) based on our model are within ±5% of the experimentally measured ones (the measured value is obtained by counting the pixels in the image, and the individual pixel size is calibrated by a rule in the same frame) (Figure 4-1b).

Then, advance distance was integrated into printing chessboard patterns (Figure 4-1c). We printed two types of chessboards with different single unit width (10×10 for Figure 4-1 d1 and 5×5 for d2 & d3). The figures with red outline showcased the printing errors when the switching point was at the edge of the pattern. The figures with green outline detailed the interface error between two chessboard units when the switching point was in the pattern. The figures with blue outline detailed deposition error at the intersections of four chessboard units. Figure 4-1 d1 & d2 were both the results with unoptimized printing paths. It can be found that when the chessboard unit is large, it showed relatively good fidelity at macro scale. However, in terms of the local detail maps, they have the same error offsets (2.7±0.5mm). Figure 4-1 d2 & d3 showed the results before and after optimization, and it was evident that the optimized results had better reproduction in local details and smaller error (±0.5mm). Subsequently, we overlaid the details of the two (Figure 4-1e) to compare the area difference between the design and printed pattern, and the optimized strategy showed considerably reduction of the error by 73% 66%

and 70% respectively. In addition, when using different nozzle heights and diameters, it was also found that the printing fidelity was improved by introducing the advance distance (Figure 4-1f). This indicated that our method was compatible to different printing conditions.

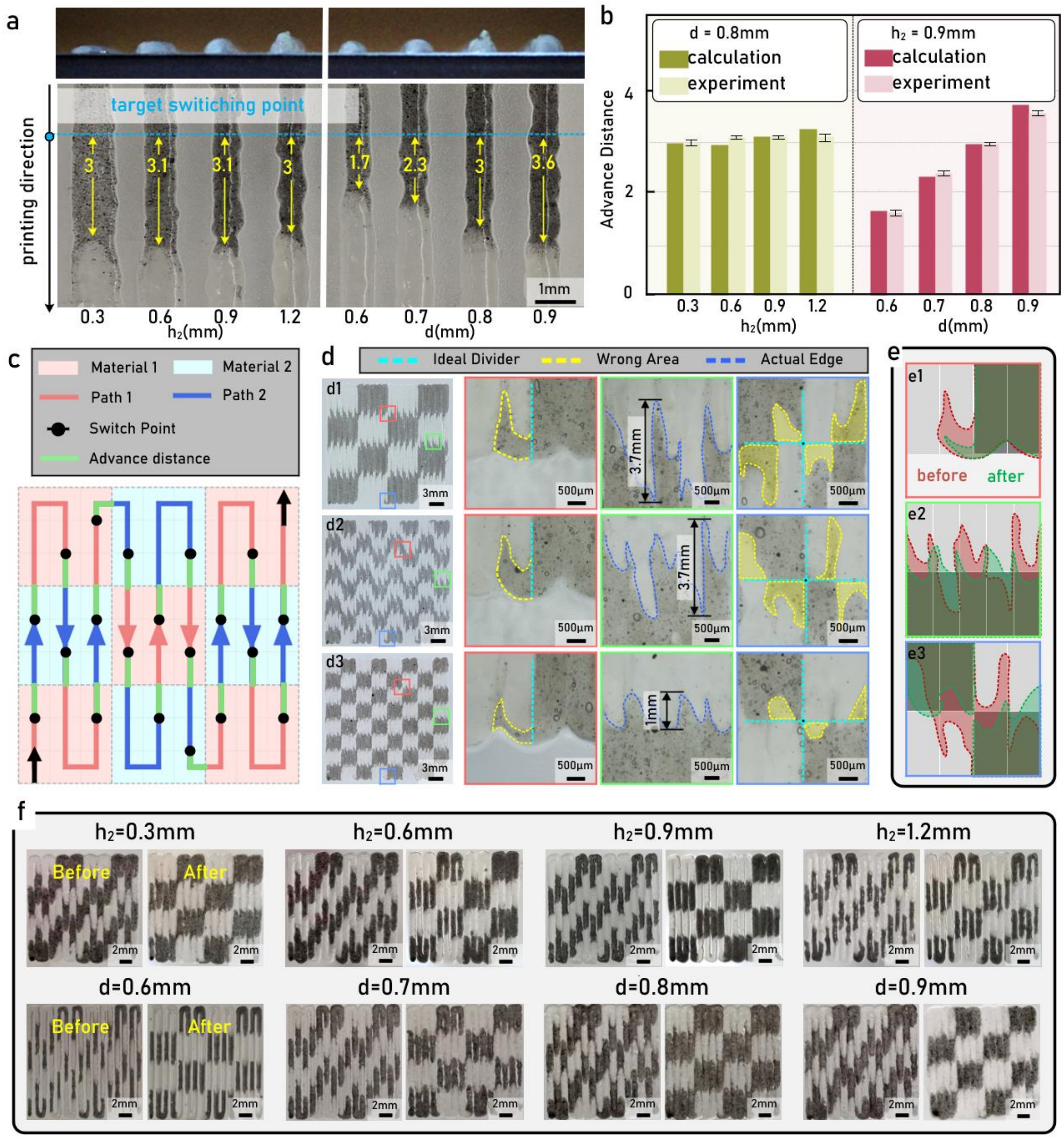

Figure 4-1 a) *examples of the switching delay in the printing direction when printing with different nozzle heights;* ***b)*** *comparison of the calculated advance distance and obtained experimentally with different combinations of nozzle heights and diameters; mean ± standard deviation,* $n = 5$*;* ***c)*** *Schematic that explains how a chess board pattern was optimized with advance distance;* ***d)*** *Printed chessboards with and without optimization: d1) unoptimized chessboard in unit of* $10\,mm \times 10\,mm$*; d2)* *unoptimized chessboard in unit of* $5\ mm \times 5\ mm$; *d3) optimized chessboard in unit of* $5\ mm \times 5\ mm$; ***e)*** *Detailed comparison of the printed chessboards in unit of* $5\ mm \times 5\ mm$; ***f)*** *Printed chessboards with different nozzle heights, diameters.*

This improvement is particularly significant in minimizing the deviation between the intended deposition points and the actual results. The resulting print fidelity, especially in intricate patterns and small-sized features, shows a remarkable improvement in fidelity, affirming the importance of advance distance calculations in the optimization of single-nozzle multimaterial direct ink writing.

Problem: During the printing process, Vaseline containing carbon powder sometimes fails to extrude, even when the extrusion pressure is increased. This issue can be temporarily resolved by increasing the extrusion pressure in experiments with larger nozzle diameters, but it becomes more frequent and unsolvable in experiments with smaller nozzle diameters. We hypothesize that this is due to large carbon particles clogging the flow channel and the friction of the channel walls preventing the clogged carbon particles from being flushed out in smaller nozzles. To address this, we attempted to flush the channel with lubricant before experiments to reduce the friction between the material and the channel walls. Although the frequency of clogging decreased, it still occurred. Observing the raw carbon powder, we noticed that clumping occurred when it was mixed in, and the clumping issue was not resolved during stirring. Therefore, before adding the carbon powder to the Vaseline, we sifted it through a sieve to filter out the clumped particles, leaving only the smaller carbon particles to be added to the Vaseline. Through experiments, we found that this solution resolved the clogging issue.

4.1.2 Extrusion compensation

Using the models described above, we tested five printing cases involving switches between two fluids of different viscosities. Figure 4-2a shows the unoptimized performance with bulging and necking. With our adaptive movement speed strategy, these effects were significantly reduced, and side effects such as unwanted merging (Figure 4-2b2) or dragging (Figure 4-2b3) were also addressed. Image processing methods were used to detect linewidth variations (Figure 4-2c). The results showed that the linewidth in unoptimized paths fluctuated between 776μm and 831μm, while optimized paths maintained a more consistent linewidth of around 800μm. Thus, our optimization significantly improved print fidelity during material switching, reducing linewidth fluctuations to 10μm.

Unlike delay compensation, the optimization effect of extrusion compensation improves as the viscosity difference between the two materials increases. When the viscosities of the two materials are the same, extrusion compensation does not contribute to optimization.

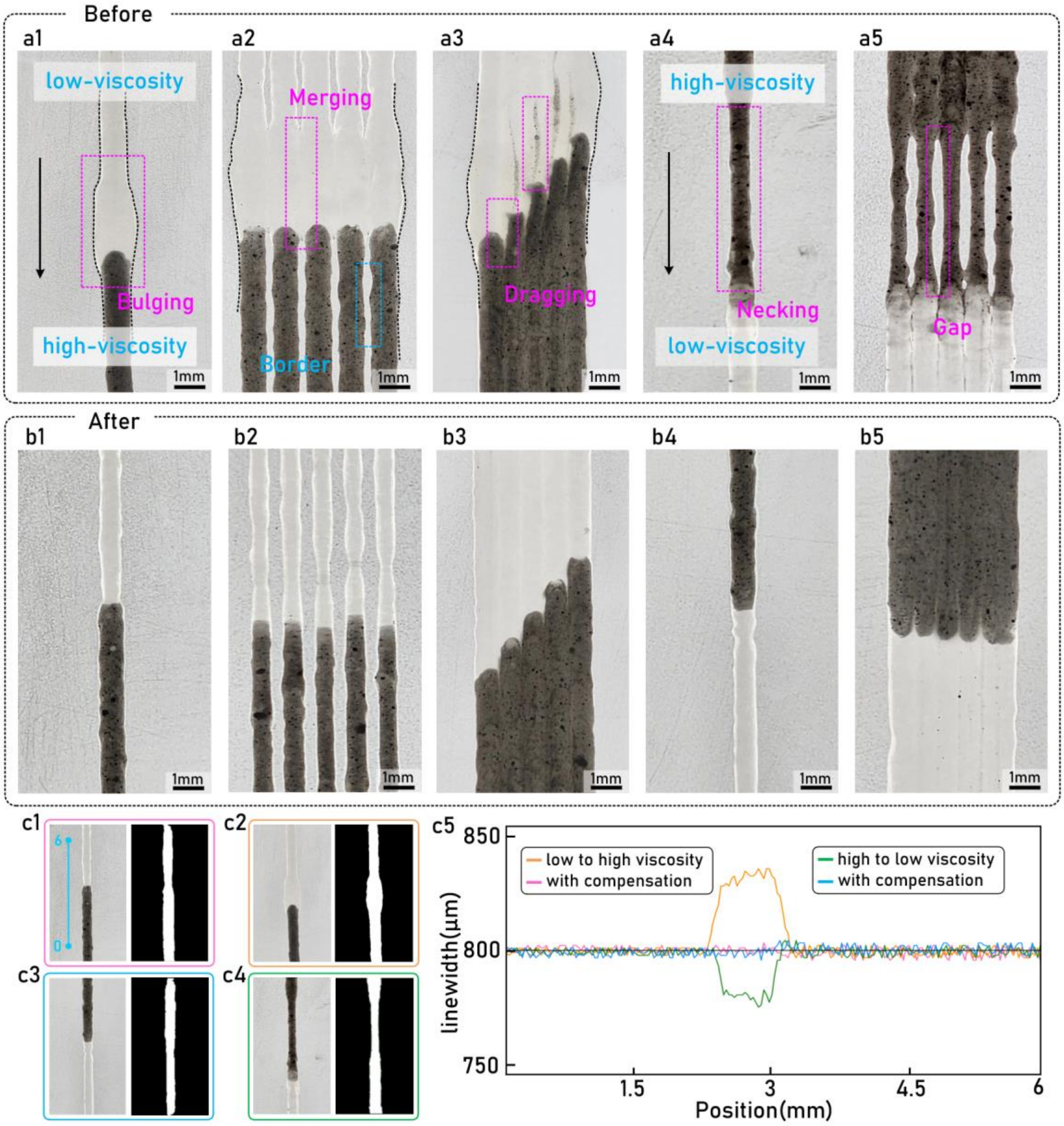

Figure 4-2 a) *Printing defects associated with switching between materials of different viscosities: a1 shows bulging at a transition from low to high viscosity without speed compensation; a2 illustrates merging defects at borders; a3 highlights dragging defects; a4 depicts necking during a transition from high to low viscosity; a5 shows a gap due to insufficient material flow;* ***b)*** *Resolved printing defect of print with compensated printing speed. b1-b5 depict the improved uniformity and reduction of defects as a result of adjusting print speed in accordance with material viscosity changes;* ***c)*** *Linewidth comparison. c1-c2 illustrate the linewidth when transitioning from low to high viscosity, c3-c4 shows the reverse. c5 quantitatively presents the linewidth variations with respect to the position.*

4.2 Printing results

4.2.1 2D pattern

Using our algorithm, we tested three different 2D patterns (Figures 4-3abc). For the University of Nottingham logo, we observed that the details of the letters and small features in the castle were well-reproduced, with minimal distortion. However, some distortion was still observed in the vertical direction due to the tailing effect during material switching. We also printed two other patterns: one with repeated and regular features (Figure 4-3b) and another with fully randomized features (Figure 4-3c). In both cases, features as small as 1mm were accurately reproduced, though vertical fidelity was slightly compromised due to the tailing effect.

Figure 4-3 Exemplars of 2D pattern prints with the slicing software that considered advance distance and in-line adjusting nozzle speed. a) *Logo of University of Nottingham;* ***b)*** *2D print of repeat pattern;* ***c)*** *2D print of random patterns.*

The fidelity of the prints was assessed using computer image processing, comparing the target and actual print results. The error for the repeated pattern (Figure 4-3b) was only 2.2%, while the error for the random pattern (Figure 4-3c) was 3.6%.

Problem: During the printing process, the width of the extruded line sometimes gradually decreases or increases, known as under-extrusion and over-extrusion. Upon investigation, we discovered that this issue was caused by the print bed not being completely parallel to the plane of the printhead movement, leading to a change in the distance between the printhead and the print bed during the printing process. In earlier experiments, since the printed patterns were small and the travel of the printhead was limited, this issue was not detected. Now, when printing larger patterns, the problem is magnified and becomes more apparent. Typically, the printer's bed can be adjusted to be parallel by manually turning several screws located beneath the plate. This process is usually referred to as bed leveling. Through repeated calibration, the parallelism between the printhead movement plane and the bed can be maintained at a high level. However, our Prusa MK3s printer's platform does not have this feature. It uses a distance sensor fixed on the printhead that scans multiple points on the print bed to calculate the height at each position and adjusts the printhead height in real-time to achieve leveling. Since we have installed a distance sensor on the printhead, we need to use another method for leveling. We chose a 4mm thick acrylic sheet as the print bed due to its good flatness. Thanks to the dual Z-axis motor design of the MK3s, we adjust the printhead movement plane in the X-axis direction by rotating one of the Z-axis motors; for the Y-axis direction, we adjust the level of the acrylic plate by placing some paper shims underneath it. To check the parallelism between the two planes, we first disable the motors in the XY direction, lower the printhead to a height where it nearly touches the acrylic sheet but can still move freely in the XY plane, and place a small piece of paper in between. As we manually move the printhead, there should be a feeling of the paper slightly rubbing against the acrylic. If the friction increases significantly or the printhead cannot move, it indicates that the printhead is slightly lower on that side. If the friction decreases significantly or the paper can slide freely, it indicates that the printhead is slightly higher.

4.2.2 3D model

Furthermore, four 3D models (two cubes and two pyramids) were designed and printed to demonstrate our protocol's performance with 3D structures. Models as shown in Figures 4-4 a3 & b3, with smaller voxel sizes, demanded higher printing precision and fidelity. The results showed that all four structures were successfully printed. The errors for the 5x5 cube were 1.5%, 2.1%, and 0.7% higher than the 3x3 cube at the top, front, and right sides, respectively. The pyramid structure with smaller voxels also showed larger errors (1.5% and 0.5% for the front and right sides) compared to the one with larger voxels.

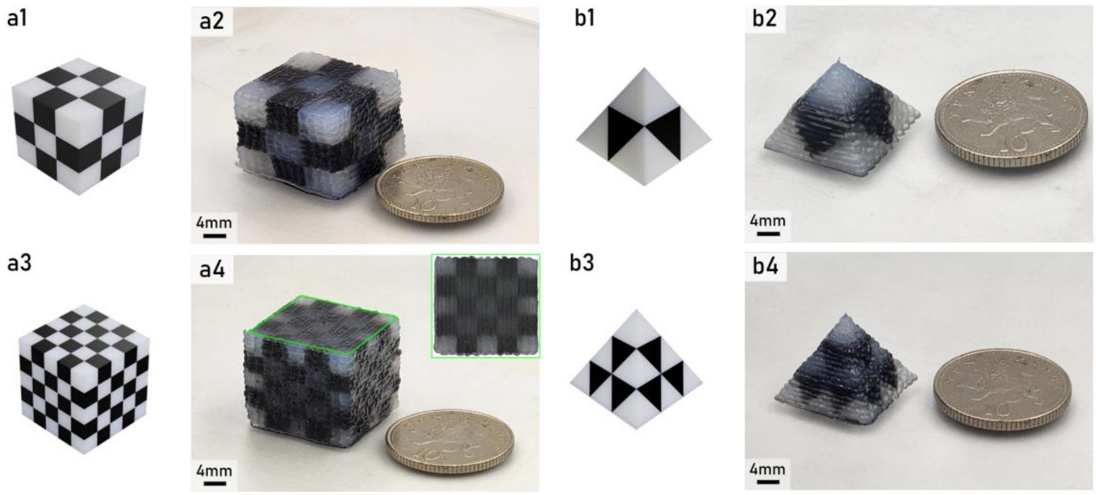

Figure 4-4 Exemplars of 3D structure prints with the slicing software that considered advance distance and in-line adjusting nozzle speed. a) *3D cube with black and white voxels;* ***b)*** *3D pyramid with black & white voxels.*

4.3 Food printing results

To demonstrate the efficacy of our proposed algorithm for 3DFP printing, we developed several extrudable edible formulations and tested our system by printing various creative structures.

4.3.1 Attractive structures

We began with 2D examples, successfully printing the University of Nottingham logo using mashed potatoes and ketchup. The choice of these materials was intended to show that the printing strategy can handle substances with varying viscosities (Figure 4-5a). The viscosity of the mashed potatoes was 3.17 Pa·s at 102 s-1 shear rate, while the modified ketchup had a viscosity of approximately 1.41 Pa·s at the same shear rate. Both mashed potatoes [127, 128] and ketchup [118] were adjusted to meet the extrusion and structural stability requirements of 3DFP. Comparative results indicate that our path planning algorithm significantly improves print quality: unoptimized results showed pattern irregularities due to switching delays, as well as visible over-extrusion and under-extrusion issues, leading to bulging and gaps during material transitions. In contrast, the optimized results displayed clear patterns and an effective blend of the two materials, demonstrating the reliability of our printing method.

We applied the algorithm to create artistic food patterns for plate decoration. We showcased a random pattern (Figure 4-5b) and a repeated pattern (Figure 4-5c), demonstrating that our method can creatively enhance the visual appeal of dishes. This visual appeal was also evident in 3D structures, such as a designed cube (Figure 4-5d). The geometric lines of the ketchup embedded in the mashed potato highlighted the printing precision and the ability to create complex designs that are challenging with traditional cooking methods, underscoring the potential of 3D food printing as a valuable tool for modern culinary practices, offering chefs and food scientists new avenues for innovation.

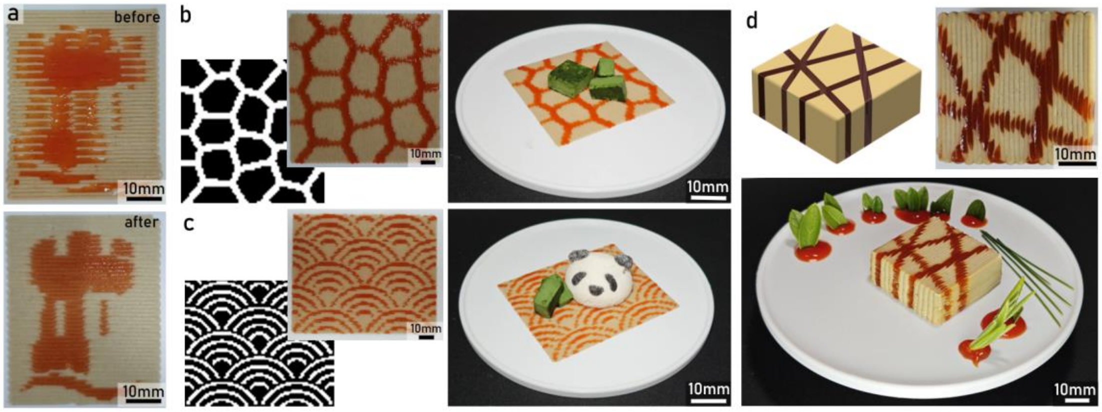

Figure 4-5 Exemplars of 2D Attractive food structures printing with the proposed strategy. a) *University of Nottingham Logo printed with and without our optimization strategy;* ***b)*** *and* ***c)*** *are artistic 2D patterns to demonstrate its application in plate decorating* ***b)*** *Random pattern;* ***c)*** *Repeated pattern;* ***d)*** *3D food printing of a cube with geometric lines.*

4.3.2 Functional structures

Despite these artistic applications, our printing strategy and algorithm also facilitate the creation of smart and healthier food options. Research has shown that it is possible to enhance taste perception by designing a spatially inhomogeneous distribution of ingredients within food products [129-133]. With carefully designed structures, it is possible to reduce the salt content by up to 30% [129] while maintaining a comparable taste profile. Drawing on existing literature, we designed and printed three different heterogeneous geometries: a cube with alternating slices (Figure 4-6a), a cube of concentric squares (Figure 4-6b), and a cube with distributed mini-cubes (Figure 4-6c). To print these exemplars, two mashed potato formulations with varying salt levels (1% w/w and 0%) were prepared and orange colorant (0.01% w/w) was added to the salt-containing formulation for introducing visual differentiation.

All printed structures were cross-sectioned to display their internal structure, confirming that both the appearance and internal structures were successfully fabricated. These examples illustrate the capabilities of our protocol, and we expect that the tools described in this thesis will provide food scientists a toolset with greater design freedom, allowing for smarter food production with fewer concerns about the capabilities and efficiency of the printer.

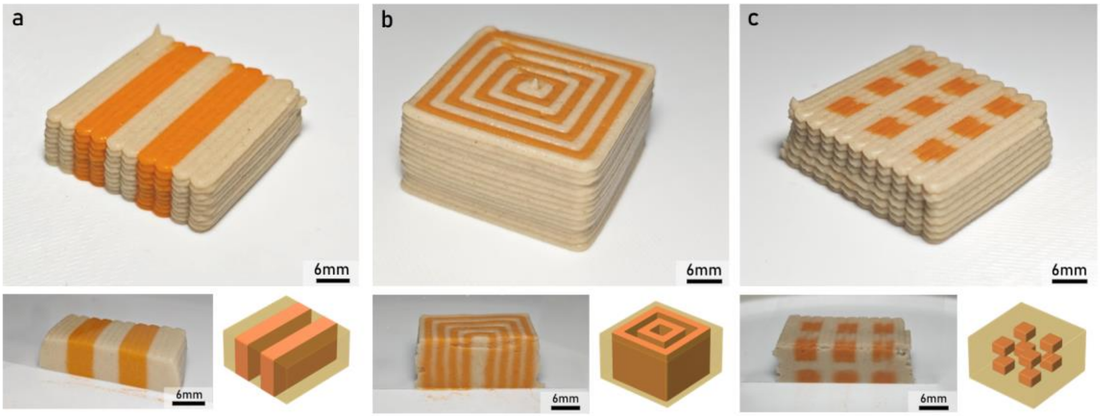

Figure 4-6 Exemplars of 3D functional food structures printing with the proposed strategy. a) *Cube with alternating slices;* ***b)*** *Cube of concentric squares;* ***c)*** *Cube with distributed mini-cubes.*

Chapter 5 Conclusions

5.1 Research outcomes

In this thesis, we applied a single-nozzle based multimaterial direct ink writing method into 3D food printing to improve printing efficiency and introduced a physical model-based path planning algorithm designed to enhance the printing fidelity.

(i) Development of Platform: We adapted the open-source 3D printer Prusa MK3S to create a specialized platform for this thesis. This modification involved integrating the single-nozzle MM-DIW system into the printer, thus allowing for controlled experiments and detailed analysis of printing processes under different conditions. Moreover, we developed some ink formulation for fidelity test and edible ink formulations for food printing.

(ii) Path Planning Algorithm: We developed and proposed a path planning algorithm that effectively compensates for the extrusion delay when switching materials. This algorithm helps in significantly reducing the switching point offset to within ±0.5 mm and stabilizes the extrusion process, which suppresses unstable extrusion behaviors such as bulging and necking.

(iii) Improvement in Printing Fidelity: We addressed the challenge of residual material in the shared channel affecting the printing process. By incorporating advanced distance calculations and real-time adjustments to nozzle movement speed in order to address issues related to delayed deposition and extrusion flow instability when switching between different materials, the errors were minimized at material switching points. The implementation of the approach showed a substantial improvement in printing fidelity. Our method demonstrated an improvement in printing fidelity, yielding a 27±11% improvement, enhancing the overall quality and reliability of the printed food products.

(iv) Experimental Validation: The models and strategies were validated through the printing of intricate patterns and geometries. The results demonstrated that the optimized algorithm significantly reduces discrepancies between the designed and actual printed patterns, achieving high fidelity in detailed and small-sized features.

(v) Open-Source Slicing Program: We provided an open-source slicing program that integrates the advanced distance calculation and printhead movement speed adjustments. This tool empowers users to implement the developed algorithms, promoting broader application and adaptation within the 3D printing community.

We believe our approach and accompanying protocol have the potential to contribute to the advancement of single-nozzle based MM-DIW processes and multimaterial food printing, offering users effective solutions to address the relevant printing challenges.

5.2 Future works

Future research could further extend from several dimensions:

(i) Material Compatibility Studies: Deepen the research on material compatibility, especially how different food materials interact within the shared nozzle system. Investigate how various combinations of materials affect the cleaning cycles of the nozzle to reduce cross-contamination and improve food safety.

(ii) Printhead Inlets Expansion: The current system supports dual-material printing; future work could involve developing a printhead capable of handling four materials. This expansion would significantly enhance the system's flexibility and scope of application, enabling more complex food printing processes that offer a richer combination of flavors and nutrients tailored to personalized dietary needs. Research would be required on how to efficiently switch and precisely control multiple materials without increasing the nozzle size and complexity.

(iii) Advanced Fluid Dynamics Models: Develop more sophisticated models for fluid dynamics within the nozzle to predict and mitigate issues such as material mixing or shear-induced changes in food texture. This could include simulations that help predict the behavior of non-Newtonian fluids, which are common in food printing.

(iv) Real-Time Monitoring and Feedback Systems: Implement sensors and feedback mechanisms to monitor the printing process in real-time. This could lead to advancements in automatically correcting errors in material deposition, adjusting parameters to maintain consistency, and improving overall printing efficiency.

(v) Customized Nutrient Optimization: Explore the potential for using this technology to customize food products based on individual dietary requirements. This could involve integrating nutrition software with the 3D printing software to create personalized meals that meet specific health needs.

Through these approaches, the performance and practicality of single-nozzle multimaterial 3D food printing technology can be further advanced.

Reference

[1] J.O. Hardin, T.J. Ober, A.D. Valentine,J.A. Lewis, Microfluidic Printheads for Multimaterial 3D Printing of Viscoelastic Inks, Advanced Materials 2015, 27, 3279.

[2] M.A. Skylar-Scott, J. Mueller, C.W. Visser,J.A. Lewis, Voxelated soft matter via multimaterial multinozzle 3D printing, Nature 2019, 575, 330.

[3] C.P. Lee, M.J.Y. Ng, N.M.Y. Chian,M. Hashimoto, Multi-material Direct Ink Writing 3D Food Printing using Multi-channel Nozzle, Future Foods 2024, 10, 100376.

[4] F. Committee, *ISO/ASTM52900 Additive Manufacturing – General Principles – Terminology [Internet]; ASTM International: West Conshohocken, PA, USA, 2015*.

[5] J.A. Lewis, Direct ink writing of 3D functional materials, Advanced Functional Materials 2006, 16, 2193.

[6] A. Maguire, N. Pottackal, M.A.S.R. Saadi, M.M. Rahman,P.M. Ajayan, Additive manufacturing of polymer-based structures by extrusion technologies, Oxford Open Materials Science 2021, 1, itaa004.

[7] M. Schaffner, J.A. Faber, L. Pianegonda, P.A. Ruhs, F. Coulter,A.R. Studart, 3D printing of robotic soft actuators with programmable bioinspired architectures, Nature Communications 2018, 9, 878.

[8] M.K. Hausmann, P.A. Rühs, G. Siqueira, J. Läuger, R. Libanori, T. Zimmermann,A.R. Studart, Dynamics of Cellulose Nanocrystal Alignment during 3D Printing, Acs Nano 2018, 12, 6926.

[9] Z.M. Gu, J.Z. Fu, H. Lin,Y. He, Development of 3D bioprinting: From printing methods to biomedical applications, Asian Journal of Pharmaceutical Sciences 2020, 15, 529.

[10] M.A.S.R. Saadi, A. Maguire, N.T. Pottackal, M.S.H. Thakur, M.M. Ikram, A.J. Hart, P.M. Ajayan,M.M. Rahman, Direct Ink Writing: A 3D Printing Technology for Diverse Materials, Advanced Materials 2022, 34, 2108855.

[11] K. Li, H. Wei, W.G. Liu, H. Meng, P.X. Zhang,C.Y. Yan, 3D printed stretchable capacitive sensors for highly sensitive tactile and electrochemical sensing, Nanotechnology 2018, 29, 185501.

[12] S.Z. Guo, K.Y. Qiu, F.B. Meng, S.H. Park,M.C. McAlpine, 3D Printed Stretchable Tactile Sensors, Advanced Materials 2017, 29, 1701218.

[13] Y.C. Fang, Y.H. Guo, B.Y. Wu, Z.B. Liu, M. Ye, Y.Y. Xu, M.K. Ji, L. Chen, B.C. Lu, K.J. Nie, Z.X. Wang, J.B. Luo, T. Zhang, W. Sun,Z. Xiong, Expanding Embedded 3D Bioprinting Capability for Engineering Complex Organs with Freeform Vascular Networks, Advanced Materials 2023, 2205082.

[14] Z.Q. Gao, J. Yin, P. Liu, Q. Li, R.A. Zhang, H.Y. Yang,H.Z. Zhou, Simultaneous multi-material embedded printing for 3D heterogeneous structures, International Journal of Extreme Manufacturing 2023, 5, 035001.

[15] T.S. Wei, B.Y. Ahn, J. Grotto,J.A. Lewis, 3D Printing of Customized Li-Ion Batteries with Thick Electrodes, Advanced Materials 2018, 30, 1703027.

[16] A.J. Blake, R.R. Kohlmeyer, J.O. Hardin, E.A. Carmona, B. Maruyama, J.D. Berrigan, H. Huang,M.F. Durstock, 3D Printable Ceramic-Polymer Electrolytes for Flexible

High-Performance Li-Ion Batteries with Enhanced Thermal Stability, Advanced Energy Materials 2017, 7, 1602920.

[17] V.G. Rocha, E. García-Tuñón, C. Botas, F. Markoulidis, E. Feilden, E. D'Elia, N. Ni, M. Shaffer,E. Saiz, Multimaterial 3D Printing of Graphene-Based Electrodes for Electrochemical Energy Storage Using Thermoresponsive Inks, Acs Applied Materials & Interfaces 2017, 9, 37136.

[18] K. Shen, J.W. Ding,S.B. Yang, 3D Printing Quasi-Solid-State Asymmetric Micro-Supercapacitors with Ultrahigh Areal Energy Density, Advanced Energy Materials 2018, 8, 1800408.

[19] Z.Y. Song, L.Q. Ren, C. Zhao, H.L. Liu, Z.L. Yu, Q.P. Liu,L. Ren, Biomimetic Nonuniform, Dual-Stimuli Self-Morphing Enabled by Gradient Four-Dimensional Printing, Acs Applied Materials & Interfaces 2020, 12, 6351.

[20] Z.H. Wang, B.Y. Zhang, W.C. Cui,N.J. Zhou, Freeform Fabrication of Pneumatic Soft Robots via Multi-Material Jointed Direct Ink Writing, Macromolecular Materials and Engineering 2022, 307, 2100813.

[21] W.J. Liu, Y.S. Zhang, M.A. Heinrich, F. De Ferrari, H.L. Jang, S.M. Bakht, M.M. Alvarez, J.Z. Yang, Y.C. Li, G. Trujillo-de Santiago, A.K. Miri, K. Zhu, P. Khoshakhlagh, G. Prakash, H. Cheng, X.F. Guan, Z. Zhong, J. Ju, G.H. Zhu, X.Y. Jin, S.R. Shin, M.R. Dokmeci,A. Khademhosseini, Rapid Continuous Multimaterial Extrusion Bioprinting, Advanced Materials 2017, 29, 1604630.

[22] I. Hassan,P.R. Selvaganapathy, Microfluidic Printheads for Highly Switchable Multimaterial 3D Printing of Soft Materials, Advanced Materials Technologies 2022, 7, 2101709.

[23] J. Mueller, J.R. Raney, K. Shea,J.A. Lewis, Architected Lattices with High Stiffness and Toughness via Multicore-Shell 3D Printing, Advanced Materials 2018, 30, 1705001.

[24] L.Q. Ren, W.X. Li, H.L. Liu, B.Q. Li, X.L. Zhou, L. Ren, Z.W. Han, Z.Y. Song,Q.P. Liu, Rotational Co-extrusion 4D printing of heterogeneous filaments to enable sophisticated shape morphing, Additive Manufacturing 2023, 73, 103661.

[25] N.M. Larson, J. Mueller, A. Chortos, Z.S. Davidson, D.R. Clarke,J.A. Lewis, Rotational multimaterial printing of filaments with subvoxel control, Nature 2023, 613, 682.

[26] Y.L. Xia, Z.L. Lu, A.J.W. Cao, K. Miao, J. Li,D.C. Li, Microstructure and mechanical property of Cf/SiC core/shell composite fabricated by direct ink writing, Scripta Materialia 2019, 165, 84.

[27] C. Paredes, F.J. Martínez-Vázquez, A. Pajares,P. Miranda, Novel strategy for toughening robocast bioceramic scaffolds using polymeric cores, Ceramics International 2019, 45, 19572.

[28] T.J. Ober, D. Foresti,J.A. Lewis, Active mixing of complex fluids at the microscale, Proceedings of the National Academy of Sciences of the United States of America 2015, 112, 12293.

[29] L.Q. Ren, Z.Y. Song, H.L. Liu, Q.H. Han, C. Zhao, B. Derby, Q.P. Liu,L. Ren, 3D printing of materials with spatially non-linearly varying properties, Materials & Design

2018, 156, 470.

[30] D. Kokkinis, F. Bouville,A.R. Studart, 3D Printing of Materials with Tunable Failure via Bioinspired Mechanical Gradients, Advanced Materials 2018, 30, 1705808.

[31] I. Hassan,P.R. Selvaganapathy, A microfluidic printhead with integrated hybrid mixing by sequential injection for multimaterial 3D printing, Additive Manufacturing 2022, 50, 102559.

[32] D. Kokkinis, M. Schaffner,A.R. Studart, Multimaterial magnetically assisted 3D printing of composite materials, Nature Communications 2015, 6, 8643.

[33] K.J. Chen, X. Kuang, V. Li, G.Z. Kang,H.J. Qi, Fabrication of tough epoxy with shape memory effects by UV-assisted direct-ink write printing, Soft Matter 2018, 14, 1879.

[34] R.R. Collino, T.R. Ray, R.C. Fleming, J.D. Cornell, B.G. Compton,M.R. Begley, Deposition of ordered two-phase materials using microfluidic print nozzles with acoustic focusing, Extreme Mechanics Letters 2016, 8, 96.

[35] J.W. Boley, K. Chaudhary, T.J. Ober, M. Khorasaninejad, W.T. Chen, E. Hanson, A. Kulkarni, J. Oh, J. Kim, L.K. Aagesen, A.Y. Zhu, F. Capasso, K. Thornton, P.V. Braun,J.A. Lewis, High-Operating-Temperature Direct Ink Writing of Mesoscale Eutectic Architectures, Advanced Materials 2017, 29, 1604778.

[36] S. Chandrasekaran, E.B. Duoss, M.A. Worsley,J.P. Lewicki, 3D printing of high performance cyanate ester thermoset polymers, Journal of Materials Chemistry A 2018, 6, 853.

[37] I.D. Robertson, M. Yourdkhani, P.J. Centellas, J.E. Aw, D.G. Ivanoff, E. Goli, E.M. Lloyd, L.M. Dean, N.R. Sottos, P.H. Geubelle, J.S. Moore,S.R. White, Rapid energy-efficient manufacturing of polymers and composites via frontal polymerization, Nature 2018, 557, 223.

[38] C. Zhu, Z. Qi, V.A. Beck, M. Luneau, J. Lattimer, W. Chen, M.A. Worsley, J.C. Ye, E.B. Duoss, C.M. Spadaccini, C.M. Friend,J. Biener, Toward digitally controlled catalyst architectures: Hierarchical nanoporous gold via 3D printing, Science Advances 2018, 4, eaas9459.

[39] H.J. Wang, C.G. Chen, F. Yang, Y.R. Shao,Z.M. Guo, Direct ink writing of metal parts with curing by UV light irradiation, Materials Today Communications 2021, 26, 102037.

[40] B.Y. Ahn, D. Shoji, C.J. Hansen, E. Hong, D.C. Dunand,J.A. Lewis, Printed Origami Structures, Advanced Materials 2010, 22, 2251.

[41] J.A. Lewis, J.E. Smay, J. Stuecker,J. Cesarano, Direct ink writing of three-dimensional ceramic structures, Journal of the American Ceramic Society 2006, 89, 3599.

[42] C. Minas, D. Carnelli, E. Tervoort,A.R. Studart, 3D Printing of Emulsions and Foams into Hierarchical Porous Ceramics, Advanced Materials 2016, 28, 9993.

[43] J.T. Muth, P.G. Dixon, L. Woish, L.J. Gibson,J.A. Lewis, Architected cellular ceramics with tailored stiffness via direct foam writing, Proceedings of the National Academy of Sciences of the United States of America 2017, 114, 1832.

[44] D.B. Kolesky, K.A. Homan, M.A. Skylar-Scott,J.A. Lewis, Three-dimensional bioprinting of thick vascularized tissues, Proceedings of the National Academy of

Sciences of the United States of America 2016, 113, 3179.

[45] D.B. Kolesky, R.L. Truby, A.S. Gladman, T.A. Busbee, K.A. Homan,J.A. Lewis, 3D Bioprinting of Vascularized, Heterogeneous Cell-Laden Tissue Constructs, Advanced Materials 2014, 26, 3124.

[46] A.E. Jakus, E.B. Secor, A.L. Rutz, S.W. Jordan, M.C. Hersam,R.N. Shah, Three-Dimensional Printing of High-Content Graphene Scaffolds for Electronic and Biomedical Applications, Acs Nano 2015, 9, 4636.

[47] M.A. Skylar-Scott, S.G.M. Uzel, L.L. Nam, J.H. Ahrens, R.L. Truby, S. Damaraju,J.A. Lewis, Biomanufacturing of organ-specific tissues with high cellular density and embedded vascular channels, Science Advances 2019, 5, eaaw2459.

[48] S. Ghosh, S.T. Parker, X.Y. Wang, D.L. Kaplan,J.A. Lewis, Direct-write assembly of microperiodic silk fibroin scaffolds for tissue engineering applications, Advanced Functional Materials 2008, 18, 1883.

[49] S. Tagliaferri, A. Panagiotopoulos,C. Mattevi, Direct ink writing of energy materials, Materials Advances 2021, 2, 540.

[50] J.Y. Chen, L.R. Xu, M.J. Yang, X.C. Chen, X.D. Chen,W. Hong, Highly Stretchable Photonic Crystal Hydrogels for a Sensitive Mechanochromic Sensor and Direct Ink Writing, Chemistry of Materials 2019, 31, 8918.

[51] E.B. Duoss, T.H. Weisgraber, K. Hearon, C. Zhu, W. Small, T.R. Metz, J.J. Vericella, H.D. Barth, J.D. Kuntz, R.S. Maxwell, C.M. Spadaccini,T.S. Wilson, Three-Dimensional Printing of Elastomeric, Cellular Architectures with Negative Stiffness, Advanced Functional Materials 2014, 24, 4905.

[52] Z.Z. Hou, H. Lu, Y. Li, L.X. Yang,Y. Gao, Direct Ink Writing of Materials for Electronics-Related Applications: A Mini Review, Frontiers in Materials 2021, 8, 647229.

[53] P.R. Wei, H.M. Leng, Q.Y. Chen, R.C. Adyincula,E.B. Pentzer, Reprocessable 3D-Printed Conductive Elastomeric Composite Foams for Strain and Gas Sensing, Acs Applied Polymer Materials 2019, 1, 885.

[54] S.L. Voon, J. An, G. Wong, Y. Zhang,C.K. Chua, 3D food printing: a categorised review of inks and their development, Virtual and Physical Prototyping 2019, 14, 203.

[55] K. Sun, T.S. Wei, B.Y. Ahn, J.Y. Seo, S.J. Dillon,J.A. Lewis, 3D Printing of Interdigitated Li-Ion Microbattery Architectures, Advanced Materials 2013, 25, 4539.

[56] J.W. Boley, E.L. White, G.T.C. Chiu,R.K. Kramer, Direct Writing of Gallium-Indium Alloy for Stretchable Electronics, Advanced Functional Materials 2014, 24, 3501.

[57] M.A. Skylar-Scott, S. Gunasekaran,J.A. Lewis, Laser-assisted direct ink writing of planar and 3D metal architectures, Proceedings of the National Academy of Sciences of the United States of America 2016, 113, 6137.

[58] W.P. Zhou, S. Bai, Y. Ma, D.L. Ma, T.X. Hou, X.M. Shi,A.M. Hu, Laser-Direct Writing of Silver Metal Electrodes on Transparent Flexible Substrates with High-Bonding Strength, Acs Applied Materials & Interfaces 2016, 8, 24887.

[59] A. Tabatabai, A. Fassler, C. Usiak,C. Majidi, Liquid-Phase Gallium-Indium Alloy Electronics with Microcontact Printing, Langmuir 2013, 29, 6194.

[60] J.B. Andrews, K. Mondal, T.V. Neumann, J.A. Cardenas, J. Wang, D.P. Parekh, Y.L.

Lin, P. Ballentine, M.D. Dickey,A.D. Franklin, Patterned Liquid Metal Contacts for Printed Carbon Nanotube Transistors, Acs Nano 2018, 12, 5482.

[61] E.B. Secor, A.B. Cook, C.E. Tabor,M.C. Hersam, Wiring up Liquid Metal: Stable and Robust Electrical Contacts Enabled by Printable Graphene Inks, Advanced Electronic Materials 2018, 4, 1700483.

[62] Y.G. Park, H.S. An, J.Y. Kim,J.U. Park, High-resolution, reconfigurable printing of liquid metals with three-dimensional structures, Science Advances 2019, 5, eaaw2844.

[63] B.Y. Ahn, E.B. Duoss, M.J. Motala, X.Y. Guo, S.I. Park, Y.J. Xiong, J. Yoon, R.G. Nuzzo, J.A. Rogers,J.A. Lewis, Omnidirectional Printing of Flexible, Stretchable, and Spanning Silver Microelectrodes, Science 2009, 323, 1590.

[64] J.J. Adams, E.B. Duoss, T.F. Malkowski, M.J. Motala, B.Y. Ahn, R.G. Nuzzo, J.T. Bernhard,J.A. Lewis, Conformal Printing of Electrically Small Antennas on Three-Dimensional Surfaces, Advanced Materials 2011, 23, 1335.

[65] M. Barnes, S.M. Sajadi, S. Parekh, M.M. Rahman, P.M. Ajayan,R. Verduzco, Reactive 3D Printing of Shape-Programmable Liquid Crystal Elastomer Actuators, Acs Applied Materials & Interfaces 2020, 12, 28692.

[66] H. Yuk, S.T. Lin, C. Ma, M. Takaffoli, N.X. Fang,X.H. Zhao, Hydraulic hydrogel actuators and robots optically and sonically camouflaged in water, Nature Communications 2017, 8, 14230.

[67] X. Wan, L. Luo, Y.J. Liu,J.S. Leng, Direct Ink Writing Based 4D Printing of Materials and Their Applications, Advanced Science 2020, 7, 2001000.

[68] M. del Pozo, L. Liu, M.P. da Cunha, D.J. Broer,A.P.H.J. Schenning, Direct Ink Writing of a Light-Responsive Underwater Liquid Crystal Actuator with Atypical Temperature-Dependent Shape Changes, Advanced Functional Materials 2020, 30, 2005560.

[69] M.O. Saed, C.P. Ambulo, H. Kim, R. De, V. Raval, K. Searles, D.A. Siddiqui, J.M.O. Cue, M.C. Stefan, M.R. Shankar,T.H. Ware, Molecularly-Engineered, 4D-Printed Liquid Crystal Elastomer Actuators, Advanced Functional Materials 2019, 29, 1806412.

[70] Y. Cheng, K.H. Chan, X.Q. Wang, T.P. Ding, T.T. Li, X. Lu,G.W. Ho, Direct-Ink-Write 3D Printing of Hydrogels into Biomimetic Soft Robots, Acs Nano 2019, 13, 13176.

[71] D.J. Roach, C. Yuan, X. Kuang, V.C.F. Li, P. Blake, M.L. Romero, I. Hammel, K. Yu,H.J. Qi, Long Liquid Crystal Elastomer Fibers with Large Reversible Actuation Strains for Smart Textiles and Artificial Muscles, Acs Applied Materials & Interfaces 2019, 11, 19514.

[72] C.P. Ambulo, J.J. Burroughs, J.M. Boothby, H. Kim, M.R. Shankar,T.H. Ware, Four-dimensional Printing of Liquid Crystal Elastomers, Acs Applied Materials & Interfaces 2017, 9, 37332.

[73] A. Clausen, F.W. Wang, J.S. Jensen, O. Sigmund,J.A. Lewis, Topology Optimized Architectures with Programmable Poisson's Ratio over Large Deformations, Advanced Materials 2015, 27, 5523.

[74] M. Moini, J. Olek, J.P. Youngblood, B. Magee,P.D. Zavattieri, Additive Manufacturing and Performance of Architectured Cement-Based Materials, Advanced Materials

2018, 30, 1802123.

[75] C. Zhu, T.Y.J. Han, E.B. Duoss, A.M. Golobic, J.D. Kuntz, C.M. Spadaccini,M.A. Worsley, Highly compressible 3D periodic graphene aerogel microlattices, Nature Communications 2015, 6, 6962.

[76] Y.W. Moon, I.J. Choi, Y.H. Koh,H.E. Kim, Porous alumina ceramic scaffolds with biomimetic macro/micro-porous structure using three-dimensional (3-D) ceramic/camphene-based extrusion, Ceramics International 2015, 41, 12371.

[77] B.G. Compton,J.A. Lewis, 3D-Printing of Lightweight Cellular Composites, Advanced Materials 2014, 26, 5930.

[78] Y. Kim, H. Yuk, R.K. Zhao, S.A. Chester,X.H. Zhao, Printing ferromagnetic domains for untethered fast-transforming soft materials, Nature 2018, 558, 274.

[79] J.R. Raney, B.G. Compton, J. Mueller, T.J. Ober, K. Shea,J.A. Lewis, Rotational 3D printing of damage-tolerant composites with programmable mechanics, Proceedings of the National Academy of Sciences of the United States of America 2018, 115, 1198.

[80] L. Friedrich, R. Collino, T. Ray,M. Begley, Acoustic control of microstructures during direct ink writing of two-phase materials, Sensors and Actuators a-Physical 2017, 268, 213.

[81] Z.J. Wang, Z.J. Wang, Y. Zheng, Q.G. He, Y. Wang,S.Q. Cai, Three-dimensional printing of functionally graded liquid crystal elastomer, Science Advances 2020, 6, eabc0034.

[82] Z.B. Liu, M. Zhang, B. Bhandari,Y.C. Wang, 3D printing: Printing precision and application in food sector, Trends in Food Science & Technology 2017, 69, 83.

[83] A. Dick, B. Bhandari, X.P. Dong,S. Prakash, Feasibility study of hydrocolloid incorporated 3D printed pork as dysphagia food, Food Hydrocolloids 2020, 107, 105940.

[84] E. Malone,H. Lipson, Fab@Home: the personal desktop fabricator kit, Rapid Prototyping Journal 2007, 13, 245.

[85] C.P. Lee, R. Karyappa,M. Hashimoto, 3D printing of milk-based product, Rsc Advances 2020, 10, 29821.

[86] Fundamentals of 3D Food Printing and Applications, Journal of Print and Media Technology Research 2019, 8, 184.

[87] Z.B. Liu, M. Zhang,B. Bhandari, Effect of gums on the rheological, microstructural and extrusion printing characteristics of mashed potatoes, International Journal of Biological Macromolecules 2018, 117, 1179.

[88] C. Liu, C. Ho,J. Wang, The development of 3D food printer for printing fibrous meat materials, 2017 2nd International Conference on Innovative Engineering Materials (Iciem 2017) 2018, 284, 110608.

[89] Q. Chang, M.A. Darabi, Y.Q. Liu, Y.F. He, W. Zhong, K. Mequanint, B.Y. Li, F. Lu,M.M.Q. Xing, Hydrogels from natural egg white with extraordinary stretchability, direct-writing 3D printability and self-healing for fabrication of electronic sensors and actuators (vol 7, pg 24626, 2019), Journal of Materials Chemistry A 2019, 7, 24641.

[90] T.G. Johnston, C.R. Fellin, A. Carignano,A. Nelson, Additive Manufacturing of

Catalytically Active Living Material Hydrogels, Micro- and Nanotechnology Sensors, Systems, and Applications Xi 2019, 10982, 1056.

[91] P. Jiang, C.Y. Yan, Y.X. Guo, X.Q. Zhang, M.R. Cai, X. Jia, X.L. Wang,F. Zhou, Direct ink writing with high-strength and swelling-resistant biocompatible physically crosslinked hydrogels, Biomaterials Science 2019, 7, 1805.

[92] W. Wu, A. DeConinck,J.A. Lewis, Omnidirectional Printing of 3D Microvascular Networks, Advanced Materials 2011, 23, H178.

[93] Q. Fu, E. Saiz,A.P. Tomsia, Direct ink writing of highly porous and strong glass scaffolds for load-bearing bone defects repair and regeneration, Acta Biomaterialia 2011, 7, 3547.

[94] A.M. Deliormanli,M.N. Rahaman, Direct-write assembly of silicate and borate bioactive glass scaffolds for bone repair, Journal of the European Ceramic Society 2012, 32, 3637.

[95] Y.H. Chen, P.P. Han, L.J. Vandi, A. Dehghan-Manshadi, J. Humphry, D. Kent, I. Stefani, P. Lee, M. Heitzmann, J. Cooper-White,M. Darguscha, A biocompatible thermoset polymer binder for Direct Ink Writing of porous titanium scaffolds for bone tissue engineering, Materials Science & Engineering C-Materials for Biological Applications 2019, 95, 160.

[96] H.S. Ma, C. Feng, J. Chang,C.T. Wu, 3D-printed bioceramic scaffolds: From bone tissue engineering to tumor therapy, Acta Biomaterialia 2018, 79, 37.

[97] W. Kim, M. Kim,G.H. Kim, 3D-Printed Biomimetic Scaffold Simulating Microfibril Muscle Structure, Advanced Functional Materials 2018, 28, 1800405.

[98] M.J. Rodriguez, J. Brown, J. Giordano, S.J. Lin, F.G. Omenetto,D.L. Kaplan, Silk based bioinks for soft tissue reconstruction using 3-dimensional (3D) printing with and assessments, Biomaterials 2017, 117, 105.

[99] H.Q. Wei, Q.W. Zhang, Y.T. Yao, L.W. Liu, Y.J. Liu,J.S. Leng, Direct-Write Fabrication of 4D Active Shape-Changing Structures Based on a Shape Memory Polymer and Its Nanocomposite, Acs Applied Materials & Interfaces 2017, 9, 876.

[100] J.Y. Liu, O. Erol, A. Pantula, W.Q. Liu, Z.R. Jiang, K. Kobayashi, D. Chatterjee, N. Hibino, L.H. Romer, S.H. Kang, T.D. Nguyen,D.H. Gracias, Dual-Gel 4D Printing of Bioinspired Tubes, Acs Applied Materials & Interfaces 2019, 11, 8492.

[101] J.W. Choi, M.O.F. Emon, F. Alkadi, J. Lee,M. Vatani, 3D printed stretchable tactile sensors, Abstracts of Papers of the American Chemical Society 2016, 252,

[102] B.D. Chen, W. Tang, T. Jiang, L.P. Zhu, X.Y. Chen, C. He, L. Xu, H.Y. Guo, P. Lin, D. Li, J.J. Shao,Z.L. Wang, Three-dimensional ultraflexible triboelectric nanogenerator made by 3D printing, Nano Energy 2018, 45, 380.

[103] A.S. Gladman, E.A. Matsumoto, R.G. Nuzzo, L. Mahadevan,J.A. Lewis, Biomimetic 4D printing, Nature Materials 2016, 15, 413.

[104] S.Y. Li, Z.Y. Song, Y.Y. Fan, D.S. Wei,Y. Liu, Four-Dimensional Printing of Temperature-Responsive Liquid Crystal Elastomers with Programmable Shape-Changing Behavior, Biomimetics 2023, 8, 196.

[105] J. Mueller, J.R. Raney, K. Shea,J.A. Lewis, Architected Lattices with High Stiffness and Toughness via Multicore-Shell 3D Printing, Advanced Materials 2018, 30,

[106] S. Mantihal, S. Prakash,B. Bhandari, Textural modification of 3D printed dark chocolate by varying internal infill structure, Food Research International 2019, 121, 648.

[107] H.W. Kim, I.J. Lee, S.M. Park, J.H. Lee, M.H. Nguyen,H.J. Park, Effect of hydrocolloid addition on dimensional stability in post-processing of 3D printable cookie dough, Lwt-Food Science and Technology 2019, 101, 69.

[108] C. Chao, J.S. Hwang, I.W. Kim, R.Y. Choi, H.W. Kim,H.J. Park, Coaxial 3D printing of chicken surimi incorporated with mealworm protein isolate as texture-modified food for the elderly, Journal of Food Engineering 2022, 333, 111151.

[109] S.M. Kim, H.W. Kim,H.J. Park, Preparation and characterization of surimi-based imitation crab meat using coaxial extrusion three-dimensional food printing, Innovative Food Science & Emerging Technologies 2021, 71, 102711.

[110] V. Vancauwenberghe, P. Verboven, J. Lammertyn,B. Nicolaï, Development of a coaxial extrusion deposition for 3D printing of customizable pectin-based food simulant, Journal of Food Engineering 2018, 225, 42.

[111] H.J. Ko, Y. Wen, J.H. Choi, B.R. Park, H.W. Kim,H.J. Park, Meat analog production through artificial muscle fiber insertion using coaxial nozzle-assisted three-dimensional food printing, Food Hydrocolloids 2021, 120, 106898.

[112] S.M. Kim, Y. Wen, H.W. Kim,H.J. Park, Textural and sensory qualities of low-calorie surimi with carrageenan inserted as a protein substitute using coaxial extrusion 3D food printing, Journal of Food Engineering 2022, 333, 111141.

[113] Z.N. Uribe-Wandurraga, L. Zhang, M.W.J. Noort, M.A.I. Schutyser, P. García-Segovia,J. Martínez-Monzó, Printability and Physicochemical Properties of Microalgae-Enriched 3D-Printed Snacks, Food and Bioprocess Technology 2020, 13, 2029.

[114] W.Y. Jeon, J.Y. Yu, H.W. Kim,H.J. Park, Production of customized food through the insertion of a formulated nanoemulsion using coaxial 3D food printing, Journal of Food Engineering 2021, 311, 110689.

[115] I. Donderwinkel, J.C.M. van Hest,N.R. Cameron, Bio-inks for 3D bioprinting: recent advances and future prospects, Polymer Chemistry 2017, 8, 4451.

[116] J. Lipton, D. Arnold, F. Nigl, N. Lopez, D. Cohen, N. Norén,H. Lipson, Multi-material food printing with complex internal structure suitable for conventional post-processing, 2010,

[117] R. Karyappa,M. Hashimoto, Chocolate-based Ink Three-dimensional Printing (Ci3DP), Scientific Reports 2019, 9, 14178.

[118] Z.B. Liu, M. Zhang,C.H. Yang, Dual extrusion 3D printing of mashed potatoes/strawberry juice gel, Lwt-Food Science and Technology 2018, 96, 589.

[119] M. Navaf, K.V. Sunooj, B. Aaliya, P.P. Akhila, C. Sudheesh, S.A. Mir,J. George, 4D printing: a new approach for food printing; effect of various stimuli on 4D printed food properties. A comprehensive review, Applied Food Research 2022, 2, 100150.

[120] A.M.F. Ghazal, M. Zhang,Z.B. Liu, Spontaneous Color Change of 3D Printed Healthy Food Product over Time after Printing as a Novel Application for 4D Food Printing, Food and Bioprocess Technology 2019, 12, 1627.

[121] C. He, M. Zhang,C.F. Guo, 4D printing of mashed potato/purple sweet potato puree with spontaneous color change, Innovative Food Science & Emerging Technologies 2020, 59, 102250.

[122] C. Chen, M. Zhang, C.F. Guo,H.Z. Chen, 4D printing of lotus root powder gel: Color change induced by microwave, Innovative Food Science & Emerging Technologies 2021, 68, 102605.

[123] Y.M. Shi, M. Zhang,P. Phuhongsung, Microwave-induced spontaneous deformation of purple potato puree and oleogel in 4D printing, Journal of Food Engineering 2022, 313,

[124] X. Wang, M. Zhang, A.S. Mujumdar,J.Y. Li, Easy-to-swallow mooncake using 3D printing: Effect of oil and hydrocolloid addition, Food Research International 2023, 164, 112404.

[125] D.M. Kong, M. Zhang, A.S. Mujumdar,J.Y. Li, Feasibility of hydrocolloid addition for 3D printing of Qingtuan with red bean filling as a dysphagia food, Food Research International 2023, 165, 112469.

[126] S.P. Sutera,R. Skalak, The history of Poiseuille's law, Annual review of fluid mechanics 1993, 25, 1.

[127] Z.B. Liu, B. Bhandari, S. Prakash,M. Zhang, Creation of internal structure of mashed potato construct by 3D printing and its textural properties, Food Research International 2018, 111, 534.

[128] Z.B. Liu, M. Zhang, B. Bhandari,C.H. Yang, Impact of rheological properties of mashed potatoes on 3D printing, Journal of Food Engineering 2018, 220, 76.

[129] Y.L. Li, K.N. Han, Z.L. Wan,X.Q. Yang, Salt reduction in semi-solid food gel via inhomogeneous distribution of sodium-containing coacervate: Effect of gum arabic, Food Hydrocolloids 2020, 109, 106102.

[130] C.X. Sun, X.L. Zhou, Z.N. Hu, W. Lu, Y.G. Zhao,Y.P. Fang, Food and salt structure design for salt reducing, Innovative Food Science & Emerging Technologies 2021, 67, 102570.

[131] S. Nakao, S. Ishihara, M. Nakauma,T. Funami, Inhomogeneous Spatial Distribution of Aroma Compounds in Food Gels for Enhancement of Perceived Aroma Intensity and Muscle Activity during Oral Processing, Journal of Texture Studies 2013, 44, 289.

[132] M.W.J. Noort, J.H.F. Bult,M. Stieger, Saltiness enhancement by taste contrast in bread prepared with encapsulated salt, Journal of Cereal Science 2012, 55, 218.

[133] T. Pflaum, K. Konitzer, T. Hofmann,P. Koehler, Influence of Texture on the Perception of Saltiness in Wheat Bread, Journal of Agricultural and Food Chemistry 2013, 61, 10649.

Appendix (Open-source code)

```python
import cv2
import numpy as np
import copy
import math
import matplotlib.pyplot as plt

standard_speed = 600  # tomato
com_speed = 500  # tomato -> potato 土豆的气压挤番茄
com_speed2 = 500  # potato -> tomato
com_time = 0  # tomato

mesh_color = ['mistyrose', 'lightcyan']
path_color = ['lightcoral', 'royalblue', 'lightgreen']

class Point:
    def __init__(self, st_x, st_y, ed_x, ed_y, ma, forward):
        self.st_x = st_x
        self.st_y = st_y
        self.ed_x = ed_x
        self.ed_y = ed_y
        self.forward = forward
        self.ma = int(ma)
        self.sw = False
        self.length = 0.0
        self.speed = standard_speed  # tomato

    def recalculate(self):
        self.length = math.sqrt((self.ed_x - self.st_x) ** 2 + (self.ed_y - self.st_y) ** 2)

    def print(self):
        print(self.st_x, self.st_y, self.ed_x, self.ed_y, self.ma, self.forward, self.length, self.speed)


class Path:
    def __init__(self, dst, n_ma, ext_d, st_x, st_y, forward: list[list[int]]):
        self.ma = dst
        self.n_ma = n_ma
        self.ext_d = ext_d
        self.h = dst.shape[0]
```

```
        self.w = dst.shape[1]
        self.st_x = st_x
        self.st_y = st_y
        self.forward: list[list[int]] = forward  # [[0, 1], [0, -1], [1, 0]]
        self.forward_unit = self.forward
        self.nxt = np.full((self.h, self.w), -1, dtype=np.int8)
        cur_x = st_x * (self.w - 1)
        cur_y = st_y * (self.h - 1)
        while self.check(cur_x, cur_y):
            cur_x, cur_y = cur_x + self.forward[self.nxt[cur_y, cur_x]][0], \
                           cur_y + self.forward[self.nxt[cur_y, cur_x]][1]
        self.pl: list[Point] = []
        cur_x = st_x * (self.w - 1)
        cur_y = st_y * (self.h - 1)
        while self.nxt[cur_y, cur_x] < len(self.forward):
            nxt_x, nxt_y = cur_x + self.forward[self.nxt[cur_y, cur_x]][0], \
                           cur_y + self.forward[self.nxt[cur_y, cur_x]][1]
            if self.ma[cur_y, cur_x] == self.ma[nxt_y, nxt_x]:
                self.pl.append(Point(cur_x, cur_y, nxt_x, nxt_y, self.ma[cur_y, cur_x] + 1, self.nxt[cur_y, cur_x]))
            else:  # change material
                mid_x, mid_y = (cur_x + nxt_x) / 2, (cur_y + nxt_y) / 2
                self.pl.append(Point(cur_x, cur_y, mid_x, mid_y, self.ma[cur_y, cur_x] + 1, self.nxt[cur_y, cur_x]))
                self.pl.append(Point(mid_x, mid_y, nxt_x, nxt_y, self.ma[nxt_y, nxt_x] + 1, self.nxt[cur_y, cur_x]))
            cur_x, cur_y = nxt_x, nxt_y
        self.ed_x = cur_x // (self.w - 1)
        self.ed_y = cur_y // (self.h - 1)

    def recalculate_length(self):
        for i in range(len(self.pl)):
            self.pl[i].recalculate()

    def simplify_gcode(self):
        i = 1
        while i < len(self.pl):
```

```
            if self.pl[i - 1].forward == self.pl[i].forward and self.pl[i - 1].ma == self.pl[i].ma and self.pl[
                i - 1].speed == self.pl[i].speed and self.pl[i - 1].sw == self.pl[i].sw:  # tomato
                self.pl[i - 1].ed_x, self.pl[i - 1].ed_y = self.pl[i].ed_x, self.pl[i].ed_y
                self.pl.pop(i)
            else:
                i += 1
        return

    def check(self, x, y):
        for i in range(len(self.forward)):
            nxt_x, nxt_y = x + self.forward[i][0], y + self.forward[i][1]
            if 0 <= nxt_x < self.w and 0 <= nxt_y < self.h and self.nxt[nxt_y, nxt_x] == -1:
                self.nxt[y, x] = i
                return True
        self.nxt[y, x] = len(self.forward)
        return False

    def adv_shift_material(self, adv_d):
        self.simplify_gcode()
        self.recalculate_length()
        i = 1
        while i < len(self.pl):
            if self.pl[i].ma != self.pl[i - 1].ma:
                temp = adv_d
                j = i - 1
                while j >= 0 and temp > self.pl[j].length:
                    self.pl[j].ma = self.pl[i].ma
                    if self.pl[i].ma == 1:  # tomato
                        self.pl[j].speed = com_speed  # tomato
                    if self.pl[i].ma == 2:  # tomato
                        self.pl[j].speed = com_speed2  # tomato
                    temp -= self.pl[j].length
                    self.pl[j].sw = True
                    j -= 1
                if j >= 0:
                    temp2 = copy.copy(self.pl[j])
                    temp2.st_x = self.pl[j].ed_x = self.pl[j].ed_x - self.forward_unit[self.pl[j].forward][0] * temp
```

```
                    temp2.st_y = self.pl[j].ed_y = self.pl[j].ed_y - self.forward_unit[self.pl[j].forward][1] * temp
                    temp2.ma = self.pl[i].ma
                    if self.pl[i].ma == 1:  # tomato
                        temp2.speed = com_speed  # tomato
                    if self.pl[i].ma == 2:  # tomato
                        temp2.speed = com_speed2  # tomato
                    self.pl.insert(j + 1, temp2)
                    self.pl[j].sw = True
                    i += 1
            i += 1
        self.simplify_gcode()
        self.recalculate_length()

    def move(self, f, x, y, st_x, st_y, ex_v):
        f.write('G1 X%.2f Y%.2f F%d\n' % (st_x + x * self.ext_d, st_y + y * self.ext_d, ex_v))

    def movez(self, f, z):
        f.write('G1 Z%.2f\n' % z)

    def shift_material(self, f, t):
        t -= 1
        for i in range(self.n_ma):

            f.write('M42 P%d S%d\n' % (i, 1 if i == t else 0))
            if i == t and com_time != 0:  # tomato
                f.write('G4 P%d\n' % com_time)  # tomato
        # if t == 1:
        #     f.write('G1 F400\n')
        # else:
        #     f.write('G1 F550\n')

    def export_gcode(self, st_x, st_y, st_z):
        global f
        self.move(f, self.st_x * (self.w - 1), self.st_y * (self.h - 1), st_x, st_y, 1000)
        self.movez(f, st_z)
        cur_ma = -1
        for i in range(len(self.pl)):
            if cur_ma != self.pl[i].ma:
                self.shift_material(f, self.pl[i].ma)
                cur_ma = self.pl[i].ma
```

```
            self.move(f, self.pl[i].ed_x, self.pl[i].ed_y, st_x, st_y, self.pl[i].speed)
        self.shift_material(f, 0)

    def export_path_pic(self, pic_path):
        # 设置图形的大小
        plt.figure(figsize=(self.w, self.h))

        # 画出 20*20 的格子图，使用半透明灰色虚线划分
        for x in range(self.h + 1):
            plt.plot([-0.5, self.w-0.5], [x - 0.5, x - 0.5], color='gray', linestyle='--', linewidth=1, alpha=0.5)
        for x in range(self.w+1):
            plt.plot([x -0.5, x-0.5], [-0.5, self.h-0.5], color='gray', linestyle='--', linewidth=1, alpha=0.5)

        # 设置坐标轴的范围
        plt.xlim(-0.5, self.w - 0.5)
        plt.ylim(-0.5, self.h - 0.5)
        # plt.fill_between([37.5, 38.5], -0.5, 0.5, color=mesh_color[0], step='post')
        for i in range(self.w):
            for j in range(self.h):
                plt.fill_between([i - 0.5, i + 0.5], j - 0.5, j + 0.5, color=mesh_color[self.ma[j,i]], step='post')
        # 画出路径
        #  （0，0）到（0，19）
        for i in range(len(self.pl)):
            plt.plot([self.pl[i].st_x,self.pl[i].ed_x], [self.pl[i].st_y, self.pl[i].ed_y], color=path_color[self.pl[i].ma - 1], linewidth=5)
        xlim = plt.xlim()
        plt.xlim(xlim[::-1])
        # 移除坐标轴的标签
        plt.xticks([])
        plt.yticks([])

        # 保存图形到本地
        plt.savefig(pic_path)

        # 清除图形
        plt.clf()

if __name__ == "__main__":
```

```python
    f = open('./GCODE/t.gcode', 'w')
    f.write('G1 Z40 F550\n')
    n_ma = 2
    now_x = 0
    now_y = 0

    ext_d = 1.4  # 线间距
    adv_d = 2.5
    st_x = 70  # 47 105
    st_y = 70  # 70 58

    layers = 1

    # 显示图形
    plt.show()
    for i in range(layers):
        img = cv2.imread('./slice/salt/' + str(i) + '.png')
        gray = cv2.cvtColor(img, cv2.COLOR_BGR2GRAY)
        retval, img1 = cv2.threshold(gray, 150, 255, cv2.THRESH_BINARY)
        dst = cv2.flip(img1, -1)
        dst[np.where(dst == 255)] = 1
        # if i % 2 == 0:
        #     forward = [[1, 0], [-1, 0], [0, 1 if now_y == 0 else -1]]
        # else:
        #     forward = [[0, 1], [0, -1], [1 if now_x == 0 else -1, 0]]
        forward = [[1, 0], [-1, 0], [0, 1 if now_y == 0 else -1]]

        a = Path(dst, n_ma, ext_d, now_x, now_y, forward)
        now_x = a.ed_x
        now_y = a.ed_y
        a.adv_shift_material(adv_d)
        # ----------- pyramid -------------
        # a.export_gcode(st_x + i * 0.5 * ext_d, st_y + i * 0.5 * ext_d, i * 0.65 - 0.05 * (i // 6))
        # ----------- pyramid -------------

        # ----------- cubic ---------------
        a.export_gcode(st_x, st_y, i * 0.85 + 11.9)  # 4.6
        a.export_path_pic('./path/%d.png'%i)
        # ----------- cubic ---------------
    f.write('G1 Z90\n')
```